NOVA SCHOOL OF SCIENCE & TECHNOLOGY

DEPARTMENT OF PHYSICS

DIOGO ALEXANDRE RIBEIRO DE ALMEIDA

BSc in Physics Engineering

QUANTUM DOTS FOR OPTOELECTRONIC APPLICATIONS

CHARACTERIZATION OF PEROVSKITE CAPPED LEAD SULPHIDE QUANTUM DOTS THROUGH THIN-FILM TRANSISTORS

MASTER IN PHYSICS ENGINEERING

NOVA University Lisbon
February, 2025

NOVA SCHOOL OF
SCIENCE & TECHNOLOGY

DEPARTMENT OF
PHYSICS

QUANTUM DOTS FOR OPTOELECTRONIC APPLICATIONS

CHARACTERIZATION OF PEROVSKITE CAPPED LEAD SULPHIDE QUANTUM DOTS THROUGH THIN-FILM TRANSISTORS

DIOGO ALEXANDRE RIBEIRO DE ALMEIDA

BSc in Physics Engineering

Adviser: Santanu Jana
Researcher, NOVA University Lisbon

Co-adviser: Manuel Mendes
Associate Professor, NOVA University Lisbon

Examination Committee

Chair: Paulo Ribeiro
Associate Professor, FCT-NOVA

Rapporteur: Suman Nandy
Principal Researcher, FCT-NOVA

Members: Santanu Jana
Researcher, FCT-NOVA

Manuel Mendes
Associate Professor, FCT-NOVA

MASTER IN PHYSICS ENGINEERING

NOVA University Lisbon
February, 2025

QUANTUM DOTS FOR OPTOELECTRONIC APPLICATIONS

Characterization of perovskite capped Lead Sulphide Quantum Dots through Thin-Film Transistors

Copyright © Diogo Alexandre Ribeiro de Almeida, NOVA School of Science and Technology, NOVA University Lisbon.
The NOVA School of Science and Technology and the NOVA University Lisbon have the right, perpetual and without geographical boundaries, to file and publish this dissertation through printed copies reproduced on paper or on digital form, or by any other means known or that may be invented, and to disseminate through scientific repositories and admit its copying and distribution for non-commercial, educational or research purposes, as long as credit is given to the author and editor.

This document was created with the (pdf/Xe/Lua)LaTeX processor and the NOVAthesis template (v7.2.1) [1].

To all people fighting for Democracy

Acknowledgements

My deepest gratitude goes to all the personnel involved in the creation and maintenance of the CENIMAT | i3N and CEMOP research centers, particularly Professor Elvira Fortunato and Professor Rodrigo Martins, without whom I would not have been able to develop this work. Your contributions help advance scientific knowledge both in Portugal and beyond.

I would also like to thank all the professors who have guided me throughout my academic journey and contributed to my ability to complete this thesis, especially Professor André Wemans and João Cruz, for their classes.

To Mudit Jain and Greesh, you are amazing people. Learning with you in Paris was the best time of my life.

A special thank you to Santanu Jana, my supervisor, for taking a chance on advising a student from a different department, with little background in material sciences, and still providing invaluable support throughout this journey.

To Shrabani, for teaching me about perovskites.

To Deneb Menda, Cristina Teixeira, Nuno Marques and Alexandra Gonçalves for helping me around the lab.

I am also deeply grateful to Professor Manuel Mendes for his regular feedback and insights - your input has been truly appreciated.

A heartfelt thank you goes to Guilherme Ribeiro and Mariana Cortinhal for dedicating so much of their time explaining countless concepts to me and revising this project. You are one of the main reasons this work was completed.

To Susana, one of the greatest joys of my life—I am incredibly lucky to have met you.

I also want to extend my heartfelt thanks to Gonçalo Mestre and Pedro Guerra for being amazing friends over the past five years.

Finally, I would like to thank my family and friends for their unwavering emotional support, particularly my sister, whom I love dearly, and my two lifelong friends, Afonso Santos and Dinis Campos, for putting up with me for the past 17 years. I love you all.

”

“The science that advances in silence is the one that changes the world.”

— Possibly Pedro Nunes, XVI Mathematician, Cosmographer
(en)

Abstract

Halide perovskite materials have emerged as promising semiconductors for optoelectronic applications, including photovoltaic cells and thin-film transistors (TFTs), due to their tuneable bandgap and high carrier mobility. However, optimizing charge transport and stability in these materials remains a challenge. This thesis investigates the functionalization of lead sulphide (PbS) colloidal quantum dots (QDs) with halide perovskite ligands as a strategy to enhance charge carrier mobility and passivate surface defects in TFTs.

A comprehensive study regarding the synthesis of quantum dots through hot-injection method, followed by ligand exchange procedure from initial oleic acid chains to perovskite ones, and thin-film transistor fabrication in a staggered bottom-gate, top-contact configuration was conducted. Optical, morphological, and electronic characterizations, including optical spectroscopy, X-ray diffraction (XRD), Fourier-transform infrared spectroscopy (FTIR), scanning electron microscopy (SEM) and transistor electrical characterization measurements, were performed to evaluate the effects of perovskite functionalization on PbS QDs. The results indicate that perovskite-capped PbS QDs exhibit ambipolar and improved charge transport properties, reaching hole mobilities up to $8.81 \times 10^{-2}\,\mathrm{cm}^2 \cdot \mathrm{V}^{-1}\mathrm{s}^{-1}$ in dark conditions, by using three depositions of the semiconductor material. We also report an optimal concentration of $104\,\mathrm{mg} \cdot \mathrm{mL}^{-1}$ for the semiconductor in study, among the ones analysed. Under light conditions, we report mobilities up to $3.690 \times 10^{-1}\,\mathrm{cm}^2 \cdot \mathrm{V}^{-1}\mathrm{s}^{-1}$, at 1 spin with $104\,\mathrm{mg} \cdot \mathrm{mL}^{-1}$, making this semiconductor layer a promising candidate for next-generation semiconductor layers in TFTs.

This research contributes to the development of quantum dot-perovskite hybrid materials, offering new insights into material optimization strategies for optoelectronic device applications.

Keywords: Optoelectronics, Photovoltaics, Thin-Film Transistors, Colloidal Quantum Dots, Metal Halide Perovskite, Ligand Exchange

Resumo

Materiais de perovskite halogenada têm emergido como semicondutores promissores para aplicações optoeletrónicas, incluindo células fotovoltaicas e transístores de filme fino (TFTs), devido à sua banda proibida ajustável e elevada mobilidade dos portadores de carga. No entanto, a otimização do transporte de carga e da estabilidade destes materiais continua a ser um desafio. Esta tese investiga a funcionalização de pontos quânticos (QDs) de sulfureto de chumbo (PbS) com ligandos de perovskite halogenada como uma estratégia para aumentar a mobilidade dos portadores de carga e passivar defeitos superficiais em TFTs.

Neste trabalho foi realizado um estudo abrangente sobre a síntese de pontos quânticos através do método de injeção quente, seguido de um processo de mudança de ligandos de ácido oleico para os de perovkiste, e da fabricação de transístores de filme fino numa configuração bottom-gate staggered, top-contact. Para avaliar os efeitos da funcionalização com perovskite nos QDs de PbS, foram realizadas caracterizações óticas, morfológicas e eletrónicas, incluindo espectroscopia ótica, difração de raios X (XRD), espectroscopia de infravermelho por transformada de Fourier (FTIR), microscópio eletrónico por varrimento (SEM) e medições de caracterização elétrica dos transístores. Os resultados indicam que os QDs de PbS funcionalizados com perovskite apresentam propriedades melhoradas de transporte de carga, atingindo mobilidades de $8.81 \times 10^{-2}\,\mathrm{cm}^2 \cdot \mathrm{V}^{-1}\mathrm{s}^{-1}$ utilizando três deposições do material semicondutor, tendo uma concentração maximizante de 104 $\mathrm{mg} \cdot \mathrm{mL}^{-1}$. Para condições de iluminação, reportamos mobilidades de até $3.690 \times 10^{-1}\ \mathrm{cm}^2 \cdot \mathrm{V}^{-1}\mathrm{s}^{-1}$, utilizando uma deposição com concentração ótima de $104\ \mathrm{mg} \cdot \mathrm{mL}^{-1}$. Estes valores tornam o material semicondutor em estudo num candidato promissor para a próxima geração de camadas semicondutoras em TFTs.

Este estudo contribui para o desenvolvimento de materiais híbridos de pontos quânticos-perovskite, oferecendo novas perspetivas sobre estratégias de otimização de materiais para aplicações em dispositivos optoeletrónicos.

Palavras-chave: Optoeletrónica, Fotovoltaica, Transístores de Filme Fino, Pontos Quânticos Coloidais, Perovskite Metálica de Halogenetos, Mudança de Ligandos

Contents

List of Figures

Acronyms

CB Conduction Band *(p. 1)*

DFT Density Functional Theory *(pp. viii, 36, 37, 46)*
DMF N,N-Dimethylformamide *(pp. ix–xi, 10, 12–15, 17, 18, 48)*

FET Field-Effect Transistor *(p. 5)*
FTIR Fourier Transform Infrared Spectroscopy *(pp. x, 12, 19, 20, 36)*
FWHM Full Width at Half Maximum *(p. 19)*

IPA Isopropyl Alcohol *(p. 11)*
ITO Indium Tin Oxide *(pp. x, 11, 12, 16)*

LE Ligand Exchange *(pp. ix–xi, 3, 10–18, 21, 26–28, 30–32, 35–37, 44, 45, 47, 48, 50, 53, 54)*

MHP Metal Halide Perovskite *(p. 4)*
MIS Metal Insulator Semiconductor *(pp. 11, 12)*

NC Nanocrystals *(pp. 1–3, 11, 12, 15, 17, 19, 35)*

OA Oleic Acid *(pp. ix, x, 9, 10, 13, 15, 16, 18–20, 25, 32, 35, 36)*
ODE Octadecene *(p. 9)*

PL Photo Luminescence Spectroscopy *(p. 17)*
PTFE Polytetrafluoroethylene *(pp. 9, 10)*

QDs Quantum Dots *(pp. viii–xi, 1–5, 9–17, 19, 21, 22, 24–28, 30–33, 35–37, 44, 45, 47–50, 53, 54)*

SEM Scanning Electron Microscopy *(pp. x, 12, 21, 35)*

TFT Thin-Film Transistor *(pp. ix, x, 1, 3, 5–7, 10, 13, 22, 24, 26, 32, 35, 37)*

TMA Trimethyl-Aluminium *(p. 11)*

UV Ultraviolet *(p. 11)*

VB Valence Band *(p. 1)*

XRD X-ray diffraction *(pp. x, 12, 19, 35)*

Symbols

Al_2O_3	Aluminium Oxide *(pp. 10, 11, 22, 35, 36)*
B	Boron *(p. 11)*
C	Gate Capacitance *(pp. 6, 7, 22)*
c	Speed of Light *(p. 14)*
CH_2	Methylene *(p. 20)*
CO_2	Carbon Dioxide *(pp. 20, 36)*
CsI	Caesium Iodide *(p. 10)*
$CsPbI_2Br$	Cesium Lead Iodide Bromide *(pp. xi, 36, 37, 44, 45)*
$CsPbI_3$	Cesium Lead Iodide *(pp. ix–xi, 1, 10, 14, 20, 24, 25, 32, 33, 35)*
d	Diameter *(p. 14)*
E_g	Bandgap *(pp. 1, 2, 13, 14)*
f	Frequency *(p. 22)*
h	Planck Constant *(p. 14)*
H_2O	Water *(p. 11)*
$\hbar$	Reduced Planck's Constant *(p. 1)*
$I_{\mathbf{DS}}$	Drain to Source Current *(pp. viii, xi, 6–8, 25, 28, 30, 33, 51–54)*
$I_{\mathbf{off}}$	Off Current *(pp. 8, 28, 29, 31, 35)*
$I_{\mathbf{on}}$	On Current *(pp. 8, 28, 29, 31, 35)*
I_{photo}	Photocurrent *(p. 33)*
J	Current Density *(pp. x, 23)*

L	Transistor Channel Length *(pp. 6, 7, 11)*
$MAPbI_3$	Methylammonium Lead Iodide *(p. 4)*
$\mu_{\mathbf{FE}}$	Field-Effect Mobility *(pp. 6, 7, 29, 31)*
$\mu_{\mathbf{Lin}}$	Linear Mobility *(p. 7)*
$\mu_{\mathbf{Sat}}$	Saturation Mobility *(p. 7)*
N_2	Nitrogen *(pp. 9, 11)*
ν	Frequency of Photon *(p. 1)*
OH	Hydroxide *(p. 11)*
PbI_2	Lead Iodide *(p. 10)*
PbO	Lead Oxide *(p. 9)*
PbS	Lead Sulfide *(pp. ix–xi, 1, 3, 4, 9, 10, 13, 15–20, 24, 25, 28, 32, 33, 35–37, 44, 45, 47–50)*
P_{light}	Incident Light Power *(p. 33)*
S	Subthreshold Swing *(pp. 7, 8, 29, 31)*
Si	Silicon *(pp. 11, 22, 35)*
$V_{\mathbf{DS}}$	Drain to Source voltage *(pp. viii–xi, 5–8, 25–28, 30, 33, 51–54)*
$V_{\mathbf{GS}}$	Gate to Source voltage *(pp. viii–xi, 5–8, 22, 23, 25, 28, 30, 31, 51–54)*
$V_{\mathbf{T}}$	Threshold Voltage *(pp. ix, 5–8, 29, 31)*
W	Transistor Channel Width *(pp. 6, 7, 11)*
λ	Wavelength *(p. 14)*

1

Introduction

This thesis aims to study and characterize films of stacked Lead Sulphide (PbS) Quantum Dots (QDs) with Caesium Lead Iodide ($CsPbI_3$) ligands as the semiconductor layer in a Thin-Film Transistor (TFT). The incorporation of these ligands might enhance charge transport between QDs, as well as passivate surface defects on the Nanocrystals (NC), resulting in an overall better performance of the TFT. Among the different types of quantum dots, the ones analysed here will be solution-based colloidal nanoparticles. A great part of the experimental work used here related to the QDs fabrication itself, has already been mapped by other researchers, as our focus is to characterize the $CsPbI_3$-terminated QDs in the electronic devices, and their optimal applications method.

1.1 Quantum Dots

Quantum dots are semiconductor NC capable of electronic quantum confinement [2]. Due to their typical size being between 1 to 10 nm, which is smaller than the exciton Bohr radius, QDs have discrete energy levels, whereas their macroscale counterparts have a continuous energy range. The energy levels of these materials can also be tuned by varying the nanoparticle size, allowing a direct control over the absorption and emission properties of the semiconductor [3].

To understand their behaviour, one can conceptualize a bulk semiconductor's electronic structure as having a Valence Band (VB), the region of maximum energy electrons and a Conduction Band (CB), the least energetic unoccupied region. These bands are separated by a Bandgap (E_g) region, where no electron can be present [4], as shown in Figures 1.1 and 1.2.

In this system, an electron at the highest energy level of the VB can absorb an energy $\hbar\nu$, with $\hbar$ being the reduced Planck's constant and ν, the frequency of the photon. If this energy is higher than E_g, it will allow the electron to move into the CB, forming an electron-hole pair, stabilized by Coulomb forces, called an exciton [6]. If the radius of this newly

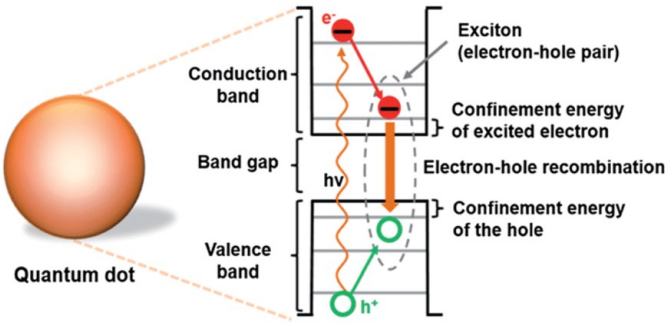

Figure 1.1: Representation of the VB and CB in a direct gap semiconductor. Absorption and emission of photons are shown. Adapted from [5].

formed quasi-particle is on the same order of magnitude as the semiconductor device under study, quantum confinement effects will arise, conditioning its absorption and emission properties, limiting them to specific energy levels. This is a crucial characteristic for a semiconductor material, as it allows for the tuning of its energy levels.

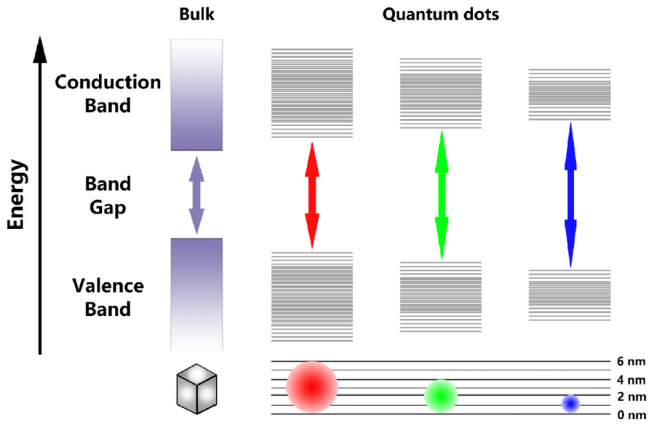

Figure 1.2: The quantum confinement effect. Comparison between bulk, nanoparticles, and molecules, showing dependence of the bandgap to particle sizes. Adapted from [7].

A remarkable aspect of these NC is their response to size decrease: as their size decreases, their E_g energy increases in value, which means that smaller crystals will resonate at higher energies, and a blueshift is noted with size decrease, as shown in Figure 1.3. For every individual spectrum, a clear, first, larger peak occurs, corresponding to the absorbance of the minimum energy required for an electron to reach the first discrete, band-edge state. Afterwards, the spectrum is continuous, showing that higher energies surpass the bandgap and are, therefore, also absorbed.

1.1.1 Lead Sulphide Quantum Dots

Lead Sulphide QDs are nanosized monocrystals with rocksalt cubic crystal structure [9] with an approximately spherical shape (truncated octahedron), capped with ligands,

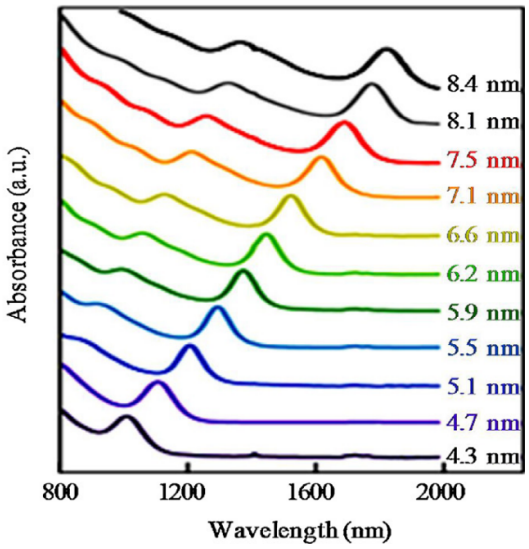

Figure 1.3: Absorbance spectra of PbS QDs over several particle diameters, ranging from 4.3 to 8.4 nm. Adapted from [8].

which help stabilize, passivate defects, control solubility, among other key features. These NC range in size between 2-10 nm, matching the condition of being smaller than Bohr's radius, giving rise to size dependent optical and electrical effects. Their tuneable bandgap (0.6–1.6 eV), broad absorption range from 200 to 2500 nm (see Figure 1.4), and high molar absorption coefficients (10^6 M^{-1} cm^{-1} at 400 nm) demonstrate the interest researchers have in the use of the nanocrystals as semiconductor layer in both TFTs and photovoltaic devices [10].

Generally, the synthesis of PbS QDs involves long chains ligands (8-18 carbons), which affect their carrier transportation and disturb their use as a reliable semiconductor layer. Therefore, in the past two decades, the size control and Ligand Exchange (LE) synthesis methods for PbS QDs have been extensively studied, the primary goal is to reduce the distance between particles, enhancing carrier transport and decreasing defect density in order to minimize recombination losses [10][11].

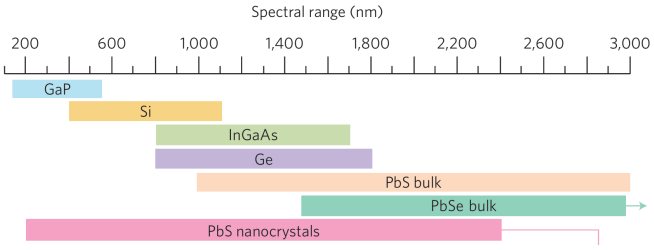

Figure 1.4: Spectral range of PbS nanocrystals. Adapted from [12].

1.2 Metal Halide Perovskite

In this chapter we will focus on describing of Metal Halide Perovskite (MHP), the structure chosen for the ligand exchange process, which will coat the above mentioned PbS QDs to improve charge carrier's transportation.

The perovskites family of crystals consists of an ABX_3 crystalline structure, pictured in Figure 1.5, where, in the case of inorganic metal halide ones, A and B are cations, with +1 and +2 charge, respectively, and a X anion, with -1 charge. An example, and one the most studied perovskites, is the Methylammonium Lead Iodide ($MAPbI_3$) compound. In the last decade, perovskite materials have been extensively studied and have re-emerged as extremely promising candidates for optoelectronics and photonic applications [13].

The distinct advantage that perovskite materials have is their ability to replace in its structure the halide component, X, and A cation to obtain different bandgap energies while maintaining a tolerance factor, indicator of the stability of a perovskite material [14], that ensures a durable crystalline structure. This property enables the synthesis of various perovskite materials with bandgap energies ranging from 1.5 to 3 eV [15].

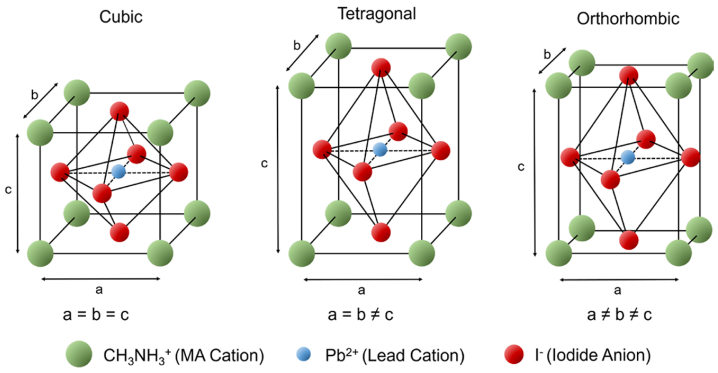

Figure 1.5: Basic structures of halide perovskite materials. Adapted from [16].

In addition to this adjustable spectral absorption range, picked among a variety of candidates for the A, X positions, MHP possesses high carrier mobility, meaning that electrons and holes move with relative ease through the material when an electric field is applied; long carrier diffusion length, which is the distance travelled by an exciton before its recombination; high absorption coefficient, which represents the normalized amount of light absorbed at a specific wavelength; and finally, simple and cost-effective fabrication methods [15] [17]. However, the use of perovskite materials as a consistent semiconductor layer in electronic devices has faced major obstacles: initially due to the volatile organic component, commonly present in the ABX_3 structure, which was overcome using inorganic perovskite. More recently due to undesired phase transitions towards lower efficiency perovskite configurations, related to the humid and thermal environment,

which still hinders commercial applications [18] [19].

1.3 Thin-Film Transistors

Thin-film transistors are Field-Effect Transistor (FET) with a channel formed as a thin-film on an insulating substrate (see Figure 1.6). They are fabricated through the deposition of an active semiconductor layer, a dielectric layer and metallic contacts onto a substrate [20]. TFTs arise as one of the answers to an increasing demand for larger elasticity from electronic devices, which would allow for a new set of devices to be made, such as electronic paper and foldable displays, whose advantages include interfacial conformability, bend ability, stretchability, and lightweight design [21]. It's with this aim that QDs with perovskite terminations can be used as an improvement for the semiconductor layer of the TFTs.

1.3.1 Thin-Film transistors structure and operation

Similarly to all field-effect transistors, TFTs use an electric field to control the flow of charge carriers in a semiconductor placed between two electrodes, the source and drain. With a third electrode, the gate, separated from the semiconductor by a dielectric layer [22].

Different layouts of TFTs can be found, each of them with their own advantages and functionalities, mostly dictated by the materials comprising the semiconductor layer (see Figure 1.7).

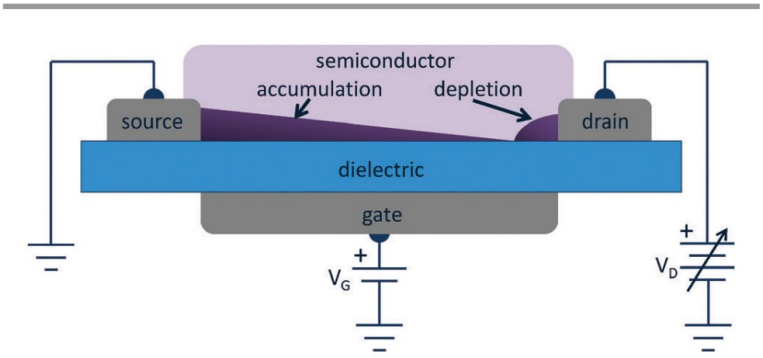

Figure 1.6: Schematic of a bottom-gate TFT, with graphic representation of the charge accumulation and depletion regions. The device is shown in the saturation regime where $V_{DS} \geq V_{GS}$ - V_T. Adapted from [23].

Focusing on the specifications of the TFTs, they can be divided into n-type or an p-type, for electrons or holes as carriers, respectively. Further categorizations are based on whether the value of its threshold voltage V_T is positive or negative.

For a n-type transistor, when a positive potential is applied across the gate-source terminals (V_{GS}), free electrons from the semiconductor material will be attracted to the

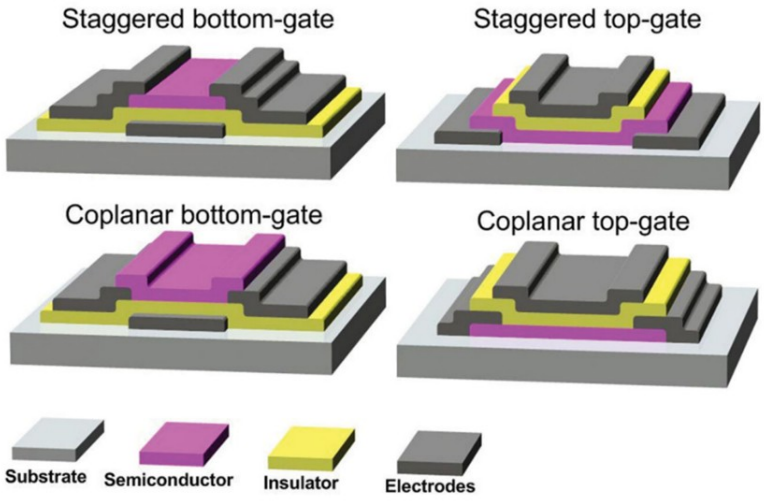

Figure 1.7: Schematics showing some of the most conventional TFT structures, according to the position of the gate electrode and to the distribution of the electrodes relatively to the semiconductor. Adapted from [22].

oxide-semiconductor interface, opening a conductive channel, this is known as the transistor being "on" (see Figure 1.8). The voltage above which the transistor is on is called threshold voltage (V_T). With the carriers located in the desired interface, when a voltage is applied across the drain-source terminals (V_{DS}), a drain to source current (I_{DS}) will flow between its terminals.

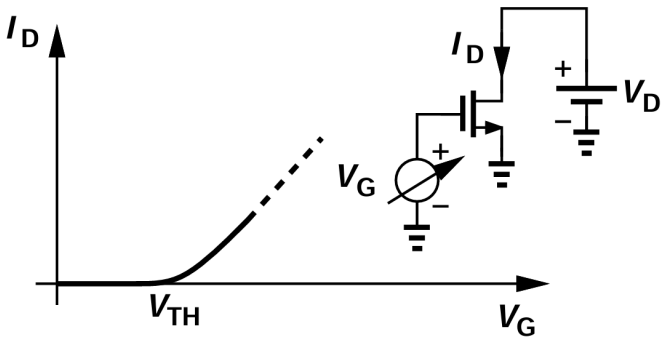

Figure 1.8: V_{DS}-V_{GS} curve, with contacts considered shorted. Inset: Field-Effect Transistor electronic diagram. Adapted from [24].

A relation between I_{DS} and V_{DS} can be established when $V_{DS} < V_{GS} - V_T$, as shown in Equation 1.1:

$$I_{DS} = \frac{1}{2}\frac{W}{L}\mu_{FE}C\left[2(V_{GS} - V_T)V_{DS} - {V_{DS}}^2\right] \tag{1.1}$$

where W and L are the width and length of the channel, respectively, μ_{FE} represents the field-effect mobility, meaning the mobility of the charge carriers in the semiconductor

and C the gate capacitance per unit area. By analysing this expression, the quadratic term can be neglected for small values of V_{DS} and revealing a linear relationship between the applied voltage and generated current (see Figure 1.9). This zone is called the triode regime, where it is assumed that the charges are uniformly distributed over the channel. However, as V_{DS} increases and $V_{DS} > V_{GS}$ - V_T, we reach a saturation region, and a new relation between applied voltage and generated current appears, as seen in Equation 1.2:

$$I_{DS} = \frac{1}{2}\frac{W}{L}\mu_{FE}C\,(V_{GS} - V_T)^2 \tag{1.2}$$

This equation is independent of V_{DS}.

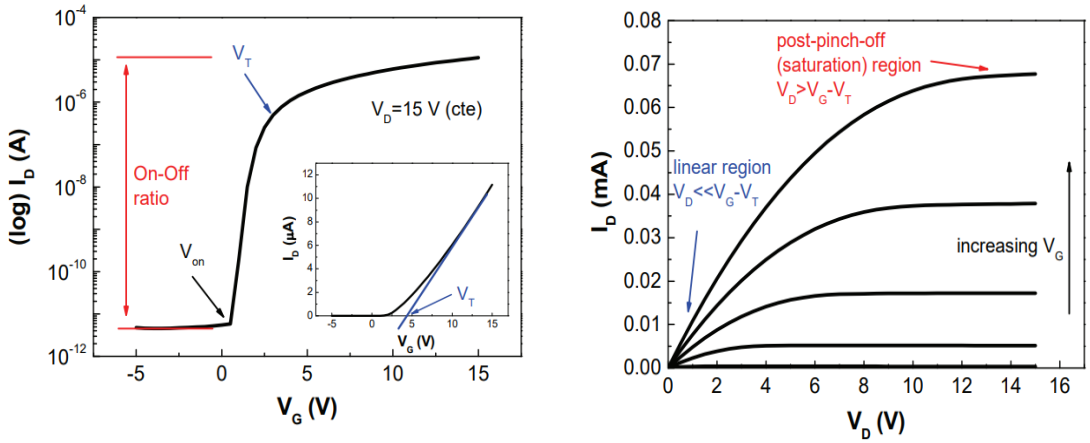

Figure 1.9: Typical transfer (left) and output (right) curves for a n-type semiconductor layer. Adapted from [25] and considering the source grounded.

As V_{DS} approaches V_{GS} - V_T, a "pinch-off" phenomenon occurs, this is related to an increase in the V_{DS} potential when seen from the source towards the drain along the length of the Field-Effect Transistor channel. This is because there is a gradual drop in voltage across the channel. The gate voltage, however, remains constant because the gate is conductive and does not carry current [24].

Some of the key characteristics which can be extracted from TFTs are: mobility μ_{FE}, on/off ratio and subthreshold swing (S).
The μ_{FE} can be extracted from both linear and saturation regime with the help of Equations 1.3 and 1.4, respectively.

$$\mu_{Lin} = \frac{\frac{\partial I_{DS}}{\partial V_{GS}}}{\frac{W}{L}\cdot C\cdot V_{DS}} \tag{1.3}$$

$$\mu_{Sat} = \frac{2}{\frac{W}{L}C}\left(\frac{\partial\sqrt{I_{DS}}}{\partial V_{GS}}\right)^2 \tag{1.4}$$

I_{on}/I_{off} ratio: ratio between the on and off current (I_{DS}) of the transistor.

V_T: Corresponds to the V_{GS} for which an accumulation layer or conductive channel is formed close to the dielectric/semiconductor interface, between the source and drain electrodes (channel region).

Subthreshold swing (S): The inverse of the maximum slope of the transfer characteristic, it indicates the necessary V_{GS} to increase V_{DS} by one decade [22]:

$$S = \left(\left| \frac{\partial \log(I_{DS})}{\partial V_{GS}} \right|_{max} \right)^{-1} \tag{1.5}$$

2

MATERIALS AND METHODS

2.1 Quantum Dot Synthesis

The synthesis of colloidal QDs was based on the work of G. Ribeiro *et al.* in [2].
A solution of lead oleate was made with 223 mg of PbO (Sigma-Aldrich, 99.999 %) as lead precursor, mixed with 1.26 mL of Oleic Acid (OA) (Sigma-Aldrich, 7 %) as ligand of the future QDs and 9 mL of Octadecene (ODE) (Sigma-Aldrich, 90 %) all mixed with a magnetic stirrer inside a three-necked round-bottom flask. Of the three flask openings, one was connected to a vacuum Schlenk line at 120 °C for about 1 h until the PbO was completely dissolved. The two others being covered with a plastic rubber and a temperature sensor to allow an entrance for the future injection and to keep track of the temperature of the solution, respectively.
Before the injection, the vacuum source was turned off, and a flow of Nitrogen (N_2), an inert gas which will prevent the interaction of the solution with undesired gases, was introduced into the flask.
For the injection, a mix of 2.5 mL degassed ODE and 105 μL of hexamethyldisilathiane, was made in a glovebox and inserted swiftly into the lead oleate solution with the help of a syringe. The success of the injection could be assessed by the quick change in colour from transparent to black.
After the injection, the heat source was immediately turned off and the flask was left to cool down until it reached a temperature of 50 °C. Afterward, the QDs were moved to a falcon tube and acetone was added to it until the 45 mL mark, shaking it. Following this, they were centrifuged for 5 minutes at 6000 rpm to precipitate and separate the QDs from the reaction by-products, the supernatant was discarded and the deposited quantum dots were dissolved in 2 mL of octane. This centrifugation and cleaning process was repeated until no visible residues were present in the supernatant. Finally, the solution was passed through a 220 nm Polytetrafluoroethylene (PTFE) filter, transferred to a glass flask, and stored in a freezer for further use. This method yielded PbS QDs with a concentration around 70 $\text{mg} \cdot \text{mL}^{-1}$.

2.2 Ligand Exchange Process

The ligand exchange process was based on the article by Xiaoliang Zhang *et al.* in [26]. To change the ligand termination from OA to $CsPbI_3$, such as displayed in Figure 2.1, and study the role of Perovskite capped PbS in a TFT, a ligand exchange process was required. In a 5 mL Eppendorf, 0.26 g of Caesium Iodide (CsI); 0.45 g of Lead Iodide (PbI_2) and 0.01 g of Ammonium acetate were dissolved with 1 mL of N,N-Dimethylformamide (DMF) . The previous solution was left stirring for 5 minutes after which, 1 mL of 35 $mg \cdot mL^{-1}$ PbS QDs were added to the stirring. After 30 minutes of stirring, the change in ligands was complete, the top octane phase was discarded, and the bottom phase washed twice by adding 1 mL of octane and vigorously shaking for 30 s, followed by discarding the top phase after phase segregation. The remaining perovskite terminated QDs present in the solution were precipitated by the addition of 1.143 mL of acetone, followed by 3 minutes of centrifugation at 8500 rpm. The supernatant was thrown away and the precipitate redissolved in 1 mL of DMF. This method yields LE QDs at a theoretical concentration of 35 $mg \cdot mL^{-1}$, even though the actual value is probably somewhat less, due to spilling and incomplete LE procedure, which were considered negligible. Images of the experimental results can be found in annex B.

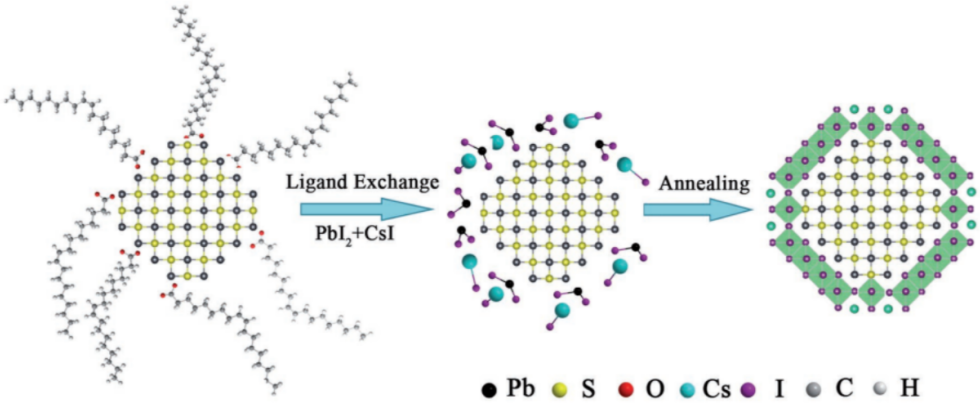

Figure 2.1: Ligand exchange procedure. Adapted from [27].

2.3 Gate Dielectric Precursor Solution Preparation

For the role of insulator between the gate and channel, a solution of aluminium oxide (Al_2O_3) was prepared based on the work of Carlos *et al.* in [28]. Aluminium nitrate nonahydrate (0.1876 g, 0.5 mmol, Roth, $\geq$ 99 %) was dissolved in 2-Methoxy Ethanol (5 mL, Sigma-Aldrich, 99.8 %), originating a solution rich in Al^{3+} ions. This was followed by the addition of Urea (0.0751 g, 12.5 mmol, Sigma-Aldrich, 99 %) to the prepared solution, which was stirred at constant speed for 1 h at room temperature. The resulting mixture was then filtered into a clean vial with a 220 nm PTFE filter.

For the atomic layer deposition measurements, the TFS-200 Beneq System was used. Al_2O_3 was deposited with Trimethyl-Aluminium (TMA) as precursor and H_2O as reactant, at 200 °C, with thicknesses of 50 nm.

2.4 Substrate Preparation

Prior to the Al_2O_3 deposition, 2.5 cm × 2.5 cm B-doped Silicon (Si) (100) wafer substrates were cut and washed. The wafers were sonicated for 15 minutes while immersed in distilled water with 3 % in volume of detergent, followed by another 15 minutes of sonication with acetone, and finally again sonicated while immersed in Isopropyl Alcohol (IPA) for 15 min. Immediately after, they were dried with a N_2 gun.

Afterwards, the wafers were submitted to a Ultraviolet (UV)/Ozone surface activation step for 15 minutes through the PSD-UV Novascan system at a distance of 2 cm and at room temperature. The dielectric thin-film was then deposited by spin-coating, where a single layer of the dielectric solution in subchapter 2.3, with a concentration of 0.1 M, was spun 3 times, using the WS–650 MZ–23NP spinner at 2000 rpm for 35 s. Afterwards, the wafers went under annealing under UV/Ozone at 150 °C for 30 min, leading to an approximately 40 nm thickness, measured through the Dektak Pro perfilometer system. The samples were later stored in vacuum in a desiccator.

The LE QDs were deposited on both Indium Tin Oxide (ITO) and in the dielectric-deposited wafers previously mentioned. The former with characterization goals in mind, and the latter for the fabrication of the final devices. For the LE QDs deposition, the wafers were subjected to a UV/Ozone surface activation step at 150 °C for 15 minutes to increase the OH^- groups. After this, they were deposited via spin-coating, where one layer was spun in a two-step procedure: first at 800 rpm for 10 s, followed by 2000 rpm for another 20 s, with an annealing step of 120 °C for 15 min.

Finally, 60 nm thick gold drain and source electrodes, with an area of 1.77×10^{-2} cm^2, were deposited using a shadow mask, with a "home-made" e-beam evaporator with W/L = 100/9 to study the Metal Insulator Semiconductor (MIS) structure, and 3 mm in diameter ones for the study of the dielectric layer. The resulting samples were stored under vacuum in a desiccator for further use.

2.5 QDs Solutions and TFTs Characterizations

UV-Visible spectroscopy was done to obtain absorbance spectra on the LE QDs using the Perkin Elmer Lambda 950 spectrophotometer and a 10 mm optical path quartz cell. The absorption spectra were measured in the 400 to 1300 nm range, covering the exciton emission frequency and the rising slope towards high energy values, and stopping before the region where organic compounds' absorbance greatly increases, which would affect the analysis of our NC. These ranges were applied to both solution and thin-film depositions.

Octane, DMF, ITO and ITO-deposited glass were used as baselines for reference for the original QDs, the LE ones, and the thin-films, respectively. Photoluminescent emission peaks of the QDs in octane, LE QDs dispersed in DMF, and in thin-films were studied using the SPEX® Fluorolog®-3FL3-22HORIBA. X-ray diffraction (XRD) studies of both octane and DMF dispersed NC in the thin-films were made using the X'Pert PRO MPD, a multipurpose diffractometer in a theta-theta configuration.

Fourier Transform Infrared Spectroscopy (FTIR) analysis was performed using the Thermo Scientific Nicolet iS50, by drop casting both the octane- and DMF-dispersed QDs onto the FTIR sample holder. Scanning Electron Microscopy (SEM) was also used to assess the surface of the distributions, through a Hitachi Regulus 8220 system.

For the capacitance measurements, the sample MIS structures were cured for 30 minutes and thereafter measured via the semiconductor parameter analyser Keysight B1500A. All current-voltage characteristics, as well as photo switching studies of the devices, were measured in continuous mode, with either back-and-forth sweeps, or one way ones, recorded in ambient conditions, inside a Faraday cage using the semiconductor parameter analyser Agilent 4155C.

Photo-switching measurements were done under 10 $\mathrm{mW \cdot cm^{-2}}$ light illumination with 0.5 s intervals between on/off cycles.

3

RESULTS AND ANALYSIS

The following chapter focuses on the data treatment, analysis and characterizations made to the PbS QDs, before and after the LE step, of the dielectric layer used for the transistor, and of the fabricated TFTs devices.

3.1 Optical Characterization

In this section, an optical analysis of PbS QDs pre and post ligand exchange is made, in octane and DMF, respectively.

3.1.1 UV-Visible Spectroscopy

The QDs absorption spectrum in Figure 3.1 matches both previous PbS spectra, and literature [11]. A noticeable emission peak appears around 1078 nm, corresponding to the bandgap transition, with an energy of E_g, followed by an increase in the QDs' absorbance. Higher-order exciton transitions at 847 nm, 526 nm and 415 nm can also be identified and used to attest the quality of the quantum dots produced.

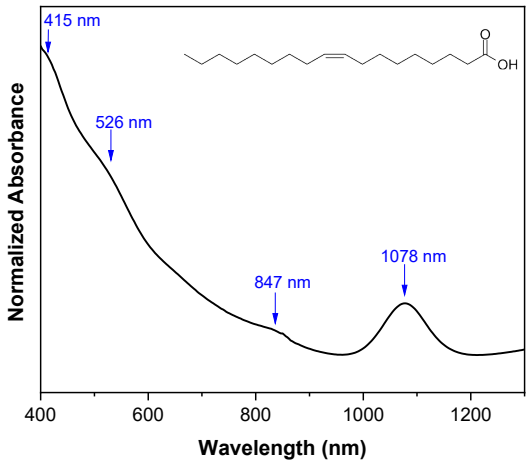

Figure 3.1: Absorption spectrum of PbS QDs in octane, with OA ligand represented.

The average diameter of the synthesized QDs will be directly related with their E_g value, this can be expressed in Equation 3.1 [29]:

$$E_g = 0.41 + \frac{1}{0.0252d^2 + 0.283d} \tag{3.1}$$

where d is the average diameter of the nanoparticles. Before heading for the diameter calculation we need the E_g value, which we compute by using Planck's equation (3.2):

$$E_g = \frac{hc}{\lambda} \tag{3.2}$$

with h being Planck's constant, c the speed of light in vacuum and λ the wavelength of the light, obtaining a bandgap of 1.15 eV and a corresponding diameter of 3.61 nm.

In the process of choosing the more adequate mean of dispersion for the LE QDs, polar aprotic solvents were considered due to their high dielectric constants which reduce the coulomb attractions of the ionic terminations of $CsPbI_3$ (Pb^{2+} and I^-). Among those, propylene carbonate and DMF were studied.

After the ligand exchange step, with propylene carbonate as medium, the main emission peak remained in the same position (1030 nm), as well as the 526 nm higher-order exciton peak observed, seen in Figure 3.2 (b) . Its constant and continuous absorption towards higher wavelength is an indicator of great uniformization of the sizes of the quantum dots, showing that propylene carbonate diminishes the chances of quantum dots aggregation.

Moreover, the lack of significant fluctuations or additional peaks in the absorption spectrum towards larger wavelengths matches a minimized amount of surface states and defects. These advantages are essential for the performance of devices.

Concerning the spectrum from the DMF solution, in Figure 3.2 (a), the main emission peak was present around 1078 nm, in the same area as the pre-ligand exchange QDs, and the second peak was seen at 544 nm.

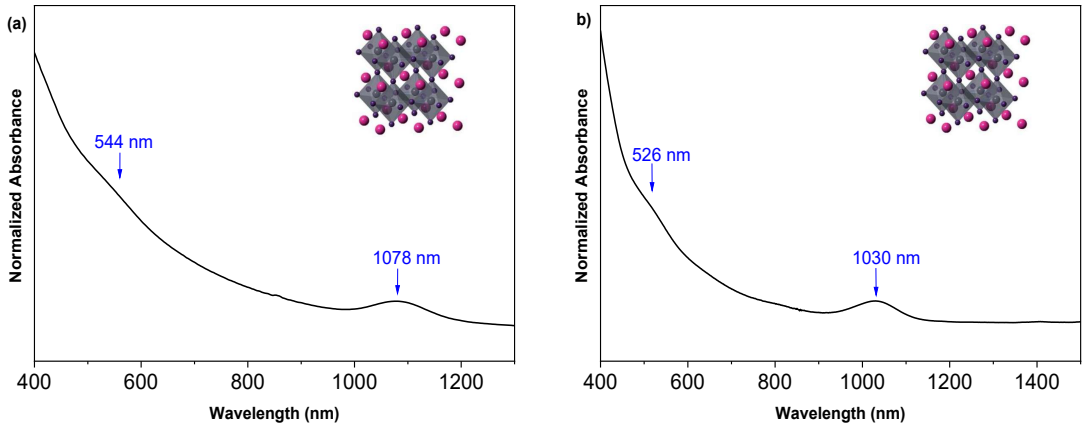

Figure 3.2: Absorbance curve of LE QDs in DMF (a) and propylene carbonate (b). With $CsPbI_3$ structure represented.

Even though not as plain towards the lower energies nor as steep in the higher energies direction, the QDs in the DMF solution may also be described by the comments on the propylene carbonate graphs, however with an overall higher chance of aggregation and size variance. A correlation between each solvent and the aggregation of QDs over time is shown in the annex A.3. The advantage of using DMF instead of propylene carbonate, even if with a slightly lower performance, it is related to the lower boiling point which allows for an easier and more efficient evaporation of the solvent in our devices, therefore from this point onward, only devices with PbS QDs in DMF solutions were produced, even though some other propylene carbonate based ones are still characterized.

An analysis of the evolution over time of both OA and LE QDs, such as in Figures 3.3 and 3.4, provides insight on the behaviour of these NC. The former shows an exciton peak that remains evident and with the same broadness as at the start of the study, with only a slight blueshift present, mainly due to surface oxidation.

In the latter, even though initially an exciton is present, this feature is largely lost after the 31st day, a sign of aggregation of the NC, due to the DMF solvent corroding the perovskite ligands, this leads to higher trap states and consequently a more inhomogeneous and inefficient charge transport between QDs.

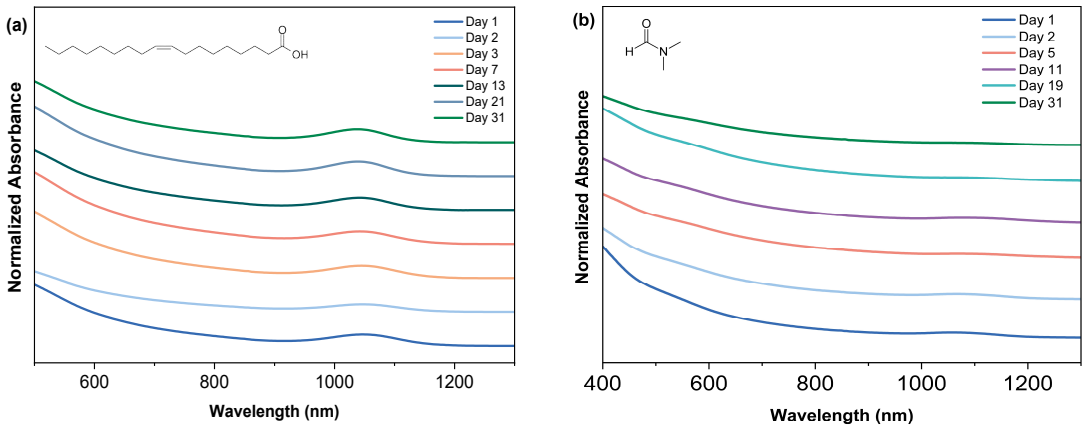

Figure 3.3: Absorbance curve of OA QDs (a) and LE QDs in DMF (b) over time. With respective ligands represented.

After the deposition in a thin-film, followed by annealing, we observe the expected result - a stabilization of the peaks' position due to the evaporation of the DMF solvent and a fixation of the QDs in the substrate, this allows us to have a more prolonged use of the later performed thin-films, at least at semiconductor level (see Figure 3.5).

The absorption spectra of the thin-films over time show that the main peaks' positions remain constant both after the LE procedure and the film deposition, an indicator of the stability of these QDs, which can be deposited onto a substrate and still possess their original features.

However, similarly to what was found in the LE solution, there is an increase in

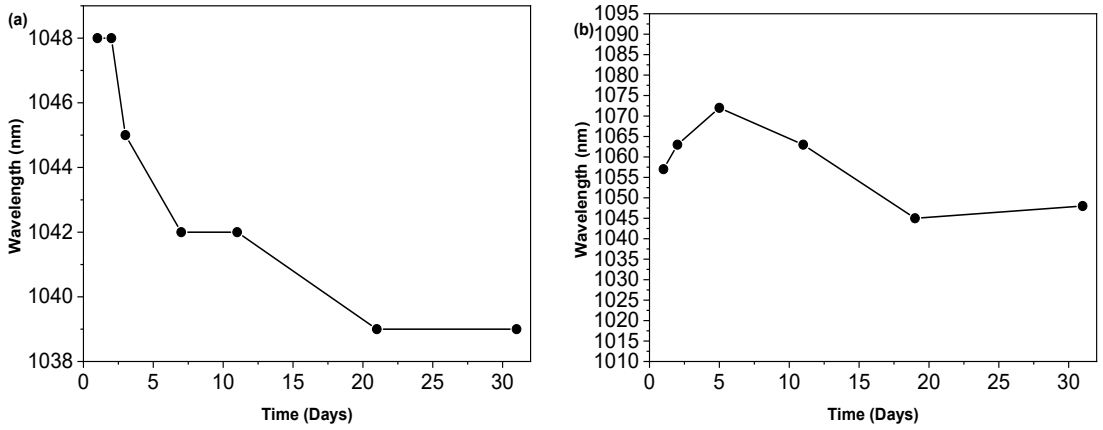

Figure 3.4: OA (a) and LE (b) QDs absorptions' peaks values over time.

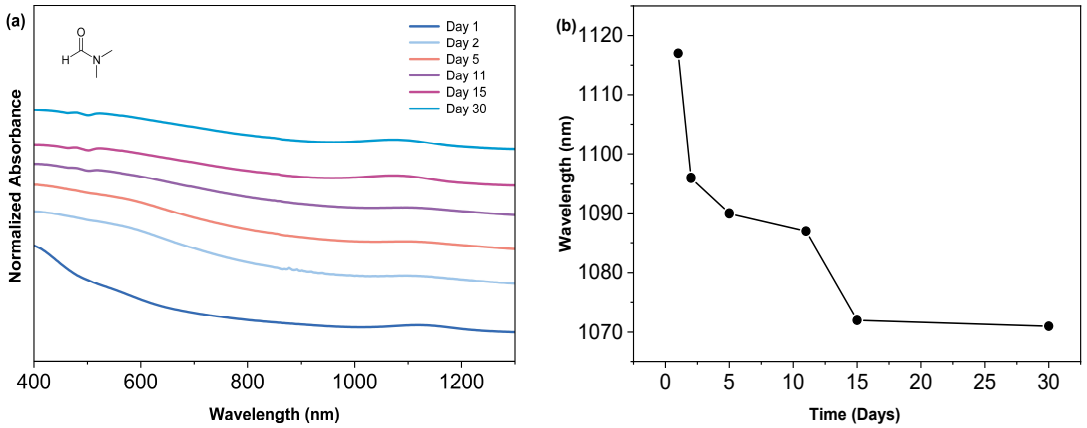

Figure 3.5: Absorbance spectrum obtained through UV-visible spectroscopy of the LE PbS QDs thin-Films deposited on ITO, through drop casting, over time (a) and PbS film absorption peak over time (b). With ligand represented.

broadness present in the main emission peak, leading to the same conclusions as in the solution case.

Finally, in Figure 3.6, the absorption spectrum of the QDs in propylene carbonate is shown, with an approximately constant peaks' position over time, and relatively uniform broadness of the peak. No noise or aggregation signs are seen towards higher wavelengths, both in a single measurement nor over time.

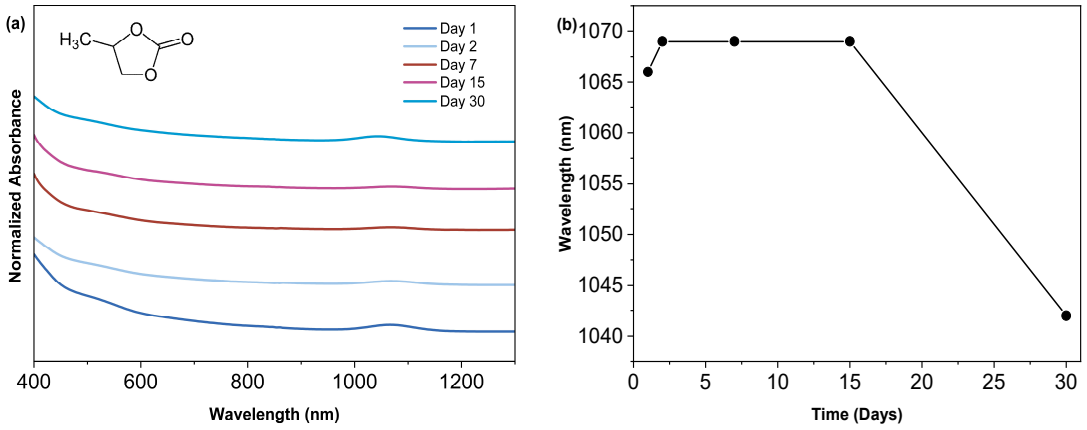

Figure 3.6: Absorbance spectrum of the LE PbS QDs in propylene carbonate solvent over time (a) and their absorption peak over time (b). With ligand represented.

3.2 Photoluminescence Spectroscopy

Photo Luminescence Spectroscopy (PL) allows the user to find information about the electronic transitions of the material being studied, through its energy emissions [30].

In Figure 3.7 (a) the emission peak is located at 1217 nm, however with a skewness to the right, a sign of aggregation which increases the emission at higher wavelengths. There is also a change in the absorption peak position to the emission one, from 1078 nm to 1217 nm, predictably due to stokes shift - a phenomena consisting in a redshift between the absorption peak of a fluorescent and semiconductor materials, and the emission one, resulting with a shift of 129 nm, and matching literature [31].

Regarding the LE PbS spectrum, the expected Gaussian-shaped peak is disturbed by an anti-peak in the 1375 nm region, due to the presence of DMF solvent, whose baseline might not have been sufficient to remove. In Figure 3.7 (b), there is also the presence of generalized noise that can be attributed to the degradation of the perovskite ligands.

Overall, both Figures 3.7 (b) and (c) show a redshift, again explained mainly by the presence of a Stokes shift when compared with the typical absorption spectra values of the LE PbS, with (b) having a peak at 1325 nm and (c) around 1425 nm.

After the 24-hour difference between both, an increase in aggregation is expected, leading to a consequent increase in volume of the NC, as presented in Figure 3.7 (c). This larger volume hampers quantum effects and explains the accentuation of the already present redshift. In Figures 3.7 (d) and (e), where the QDs are in a film and propylene carbonate, respectively, their emission spectra remain relatively smooth, with the same Stokes shift effect present, even though with less intensity for the film analysis. Their peaks are located at 1116 nm and 1272 nm, revealing consistency in its position from the pre and to the post-ligand exchange situation.

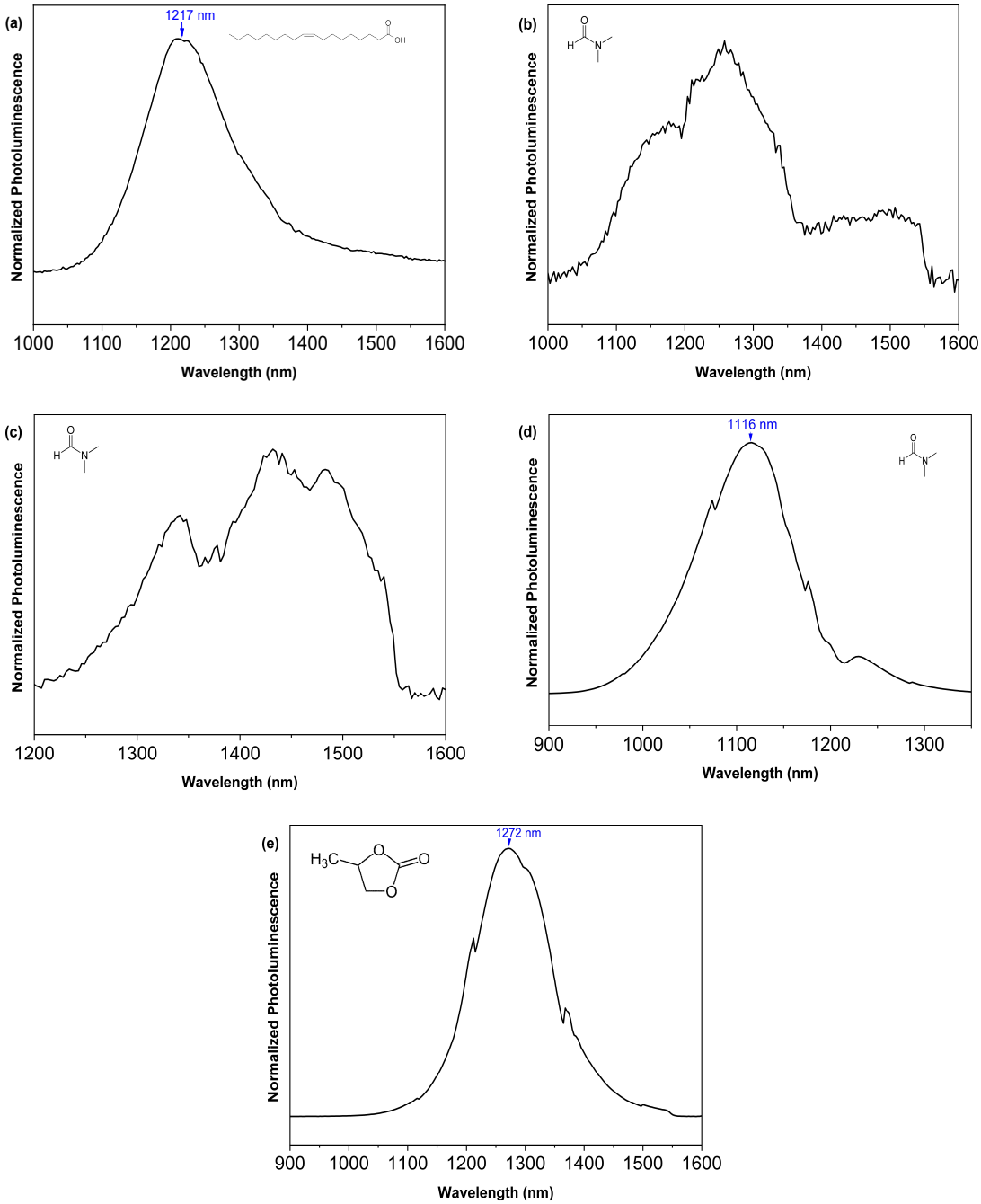

Figure 3.7: Photoluminescence emissions of (a) OA PbS in Octane; (b) and (c) LE PbS in DMF 24 h apart; (d) LE PbS in thin-film by drop casting; and (e) LE PbS in propylene carbonate. With respective ligands represented.

3.3 Morphological and Structural Characterization

3.3.1 X-ray Diffraction

X-ray diffraction allows to have a qualitative knowledge of the chemical composition of the elements being analysed, their crystallographic structure and grain size, in a non-destructive way [32].

Observing Figure 3.8 (a), it is possible to visualize diffraction peaks at 25.96°, 29.91°, 42.95°, 51.02°, 70.43°, and 78.66°, which correspond to the *Fm-3m*, planes (111), (200), (220), (311), (420), and (422), respectively. In Figure 3.8 (b), the peaks occur at 14.89°, 21.15°, 23.67°, 30.01°, 33.71°, 36.92°, and 43.05°, which match the *Pm3m*, No. 221 (100), (110), (111), (200), (210), (211), and (220) planes, respectively.

These diffraction patterns obtained for the OA QDs illustrate the same face centred cubic structure present in [11], which has been reported for bulk crystal PbS.

In Figure 3.8 (a), the exhibited peaks do not possess the same quality in terms of Full Width at Half Maximum (FWHM) as the one exhibited in previous literature. However, after the ligand exchange process, a clearer crystallography of the QDs is detected. This difference arises because of the long OA chains, which are not crystallographic but surround the NC, affecting the measurement.

In Figure 3.8 (b), a *Pm3m*, No. 221 structure is also detected [33].

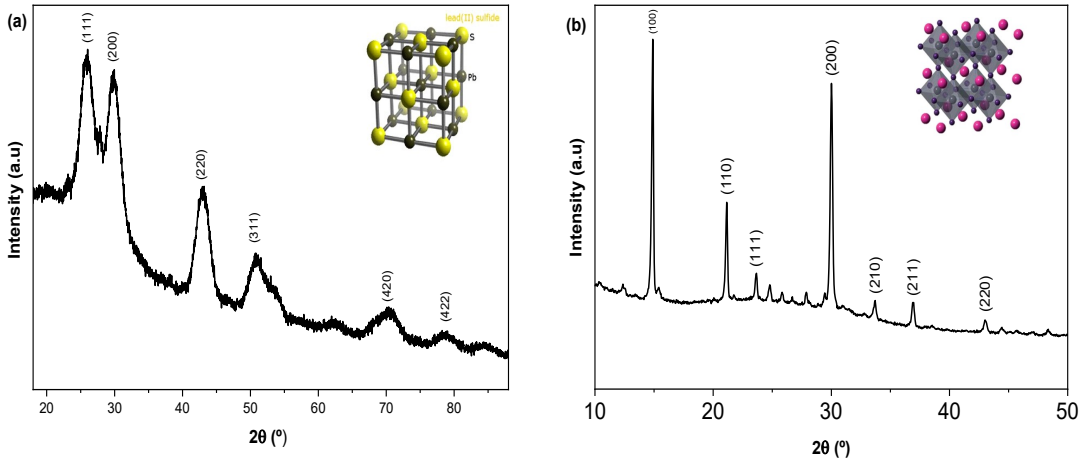

Figure 3.8: XRD diffractograms of (a) the hexane-dispersed OA PbS QDs, and (b) ligand-exchanged PbS. With ligands represented.

3.3.2 Fourier Transform Infrared Spectroscopy

A FTIR analysis allows to detect the presence of the different elements in the sample being analysed, this is achieved through the absorption as a function of wavelength spectra. The analysis can be done because different chemical groups possess different absorption wavelengths, leading to different absorption spectra's for different elements [34]. In the

PbS sample being analysed, it is expected that mostly Lead-Sulphide covalent bonds are detected, however, other elements, such as impurities will also be present and can be explained here.

The FTIR spectrum in Figure 3.9, in the 2922 cm^{-1} and 2854 cm^{-1} regions reveal the presence of alkyl chains, such as oleic acid. These peaks interestingly remain after the ligand exchange step, which can be interpreted as the oleic acid remaining in the solution due to an incomplete ligand exchange step [35].

An interesting result to comment on is the change in position of the pair of carboxylate (asymmetric and symmetric) peaks from the OA to $CsPbI_3$ capping, at both 1462 cm^{-1} and 1378 cm^{-1} to 1532 cm^{-1} and 1403 cm^{-1} [35]. A possible explanation for this phenomenon is the change in binding mode, from a bidentate binding to a monodentate one, related to an increase in the energy separation of the peaks.

A peak at 722 cm^{-1}, representing the methylene (CH_2) rocking mode, remains constant with the ligand exchange procedure [36]. Finally, the appearance of a carbon dioxide (CO_2) stretch in the $CsPbI_3$ capping is related to contamination of the sample with carbon dioxide [37].

No Lead-Sulphide bond was detected in either analysis, possibly due to their presence surrounded by ligands.

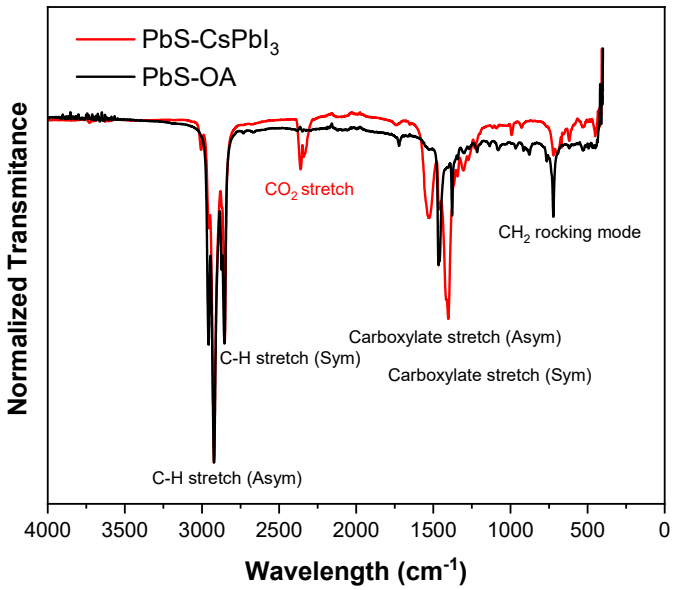

Figure 3.9: FTIR spectrum of PbS capped with $CsPbI_3$ (red) and PbS capped with oleic acid (black). Labels corresponding to each absorption are included.

3.3.3 Scanning Electron Microscopy

SEM is used to visualize the surface of a material, giving information about its texture and grain structure, in this case, the semiconductor layer used in the thin-films [38].

In Figure 3.10, it's possible to see two different sections of the LE QDs deposited through spin-coating. Their sizes are approximately uniform, a sign of uniform growth of the nanocrystals with the experimental method used in this thesis, and an important factor for consistent optoelectronic properties in the devices. Another interesting characteristic is the non-aggregation of the spun QDs, attesting to the quality of the used spinning conditions, which again permits a uniform use of the quantum confinement effects. Bright spots are zones with a higher concentration of QDs and unreacted lead iodide. In Figure 3.11 we display a binary transformation of one of the SEM images in 3.10. Here, using, the software of *ImageJ*, we have managed to study the number of clearly identified agglomerates of QDs, calculated to be 110. However, emphasizing that even though clear agglomerates are present, their sizes are relatively small to the paths which connect them.

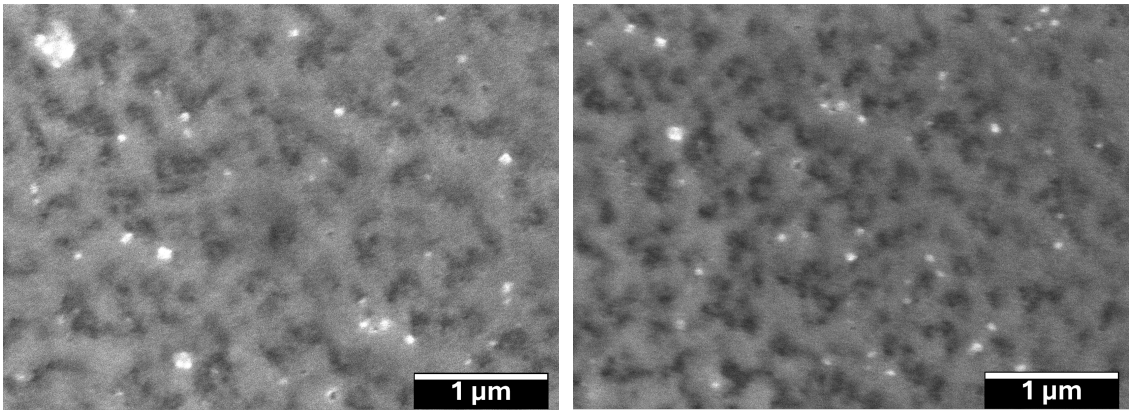

Figure 3.10: SEM images of LE QDs (grey continuous film) dispersed into glass.

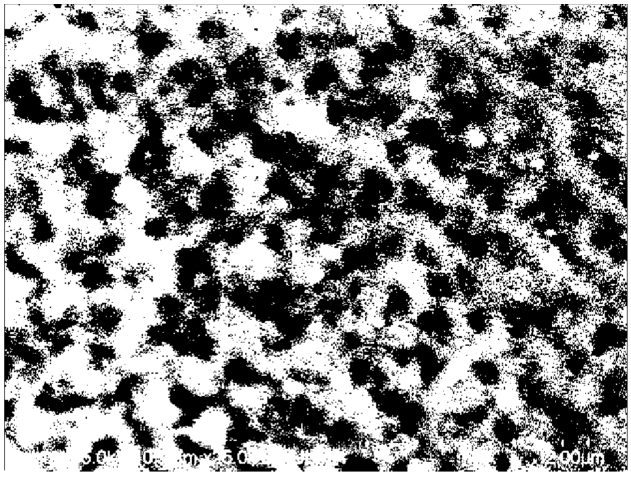

Figure 3.11: Binary transform of SEM image from Figure 3.10.

3.4 Electronic Characterization

In the following pages, an analysis of the electric characterization of the QDs and TFTs devices will be made.

3.4.1 Dielectric Layer Characterization

It is also necessary to characterize the dielectric layer of the device, as its functioning is a crucial part of the development of a TFT. The dielectric constant and breakdown field of the Al_2O_3 layer can be described through capacitance-voltage (C-V), capacitance-frequency (C-f), and current-voltage (I-V) curves.

Several attempts were performed to produce an Al_2O_3 dielectric layer capable of yielding a valid theoretical dielectric constant. The initial one spin coating deposition provided a capacitance of $0.014\,\mu\text{F}\cdot\text{cm}^2$ at 1 kHz (resulting in a dielectric constant of 0.203 with 13 nm thickness), significantly smaller than the reported values for the same procedures [28]. Among the possible explanations, we hypothesise a not uniform dispersion, with sections with a thickness below 3 nm, leading to tunnelling events. Considering the small thickness of the film, another possibility is the presence of Poole–Frenkel effects, when approaching voltages above 2 V [39]. Through atomic layer deposition we have achieved a value of $0.029\,\mu\text{F}\cdot\text{cm}^2$ for 1 kHz (dielectric constant of 1.63 with 50 nm thickness), already in the same order of magnitude as our aim, but still inferior to the expected value.

Finally, a three times deposition through spin coating was made (39 nm thickness), with the results displayed in Figures 3.12 b) and d), reaching a capacitance value of $0.154\,\mu\text{F}\cdot\text{cm}^2$ (dielectric constant of 6.78), similar to theoretic values, and confirmed by both the C-V and C-f graphs. In Figure 3.12 b) we notice hysteresis is present in the -5 V to 0 V region, attributed to the presence of defects at the interface between Si and the Al_2O_3, naturally disturbing the functioning of the completely assembled transistor [40].

The C-f graph provides insight into the evolution of the capacitance value over several frequencies, showing a diminishing trend until the 40000 Hz region, in which we have room for improvement, aiming for a more gradual transition.

Finally, the current-density (J-V_{GS}) curve, seen in Figure 3.12 c), extracted to study the leakage current, shows a maximum leakage current at 1.086×10^{-5} A, and a minimum value at 0 V of 9.072×10^{-9} A. Unfortunately, both maximum and minimum leakage currents surpass standard experimental values for approximately the same thicknesses [28].

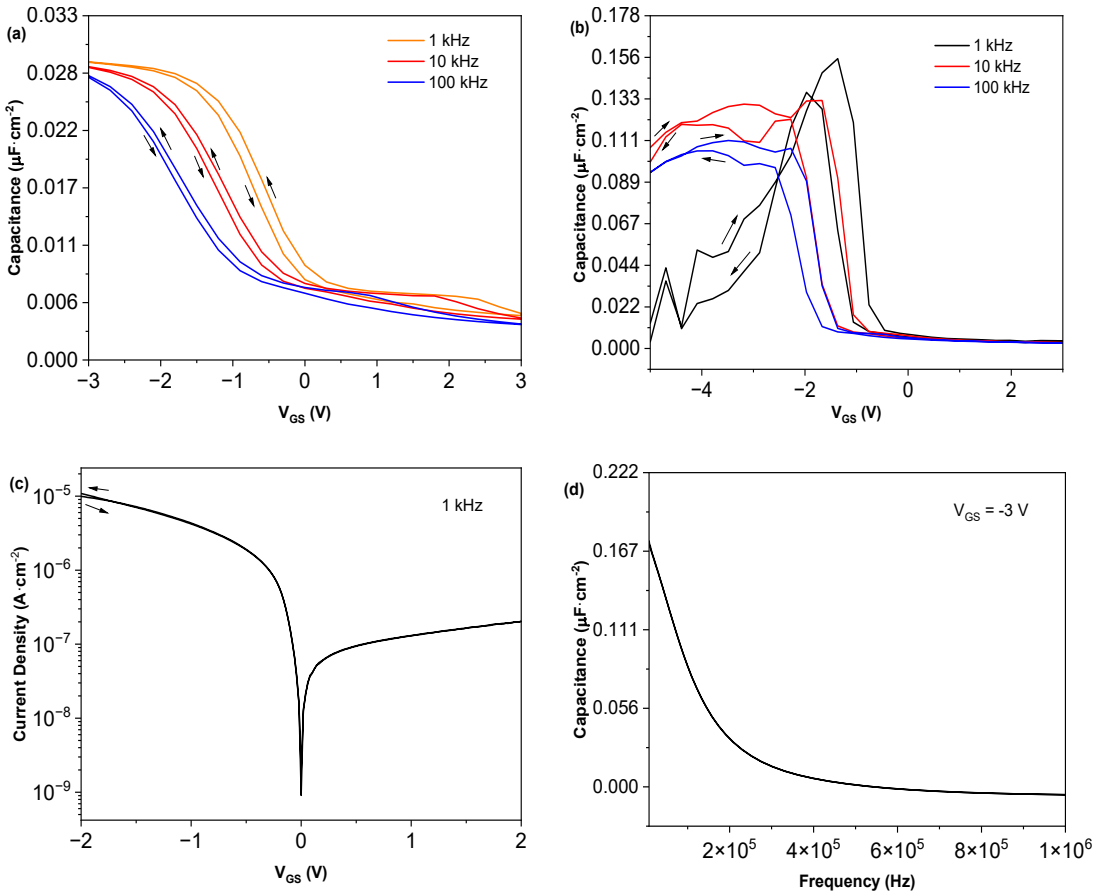

Figure 3.12: Characterization of the dielectric layer with (a) capacitance-V_{GS} graph by atomic layer deposition, (b) capacitance-V_{GS} graph with spin-coated dielectric layer (c) J-V_{GS} sweep with spin-coated dielectric, and (d) capacitance-frequency sweep with spin-coated deposition.

3.4.2 Thin-Film Transistor Characterization

The fabrication of TFTs (Figure 3.13) using the $CsPbI_3$ terminated QDs is not only in itself a way to characterize the previously mentioned QDs but allows also to pave the way for a more effective semiconductor layer. In this section we vary the number of depositions as well as the concentration of the deposited semiconductor layer, looking to find the optimal conditions for this material and method.

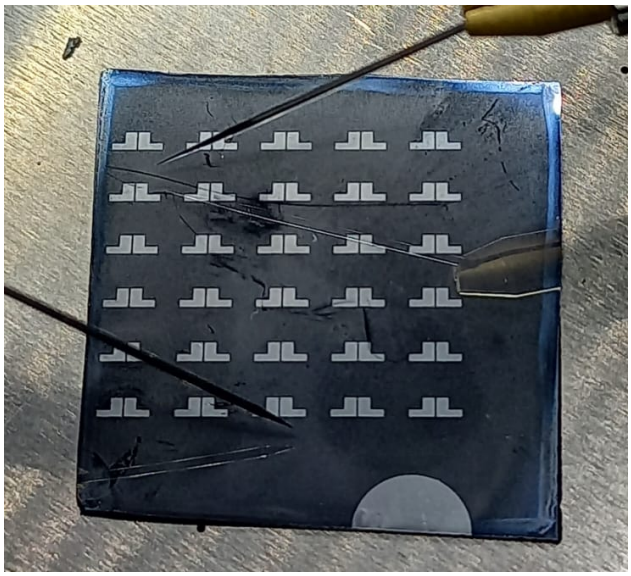

Figure 3.13: Final TFT device, using PbS QDs as the semiconductor layer with gold contacts. 2.5 cm x 2.5 cm dimensions.

3.4.2.1 I_{DS}-V_{GS} Curve

Analysing Figure 3.14, it is remarkable the consistency of shape of the curve in both positive/negative directions of the voltage, which is an indicator of low charge-trapping [41] and low ion migration [42], diminishing the presence of hysteresis in the semiconductor material, a desirable trait for an electronic device. An ambipolar behaviour is also present, although more receptive for electron conduction, this layer can be used for both hole and electrons transport. There is an increase in the output current when the QDs ligands are switched from oleic acid to $CsPbI_3$. The reason behind this is related with the higher mobility that is reported for the perovskite ligands when compared with the OA ones. Through Origin Software's functionalities, it was found that the area under the perovskite ligand's curve, related to its transport capabilities, increased from 7.394×10^{-7} a.u. to 9.484×10^{-7} a.u , or 28.26 %, a remarkable increase.

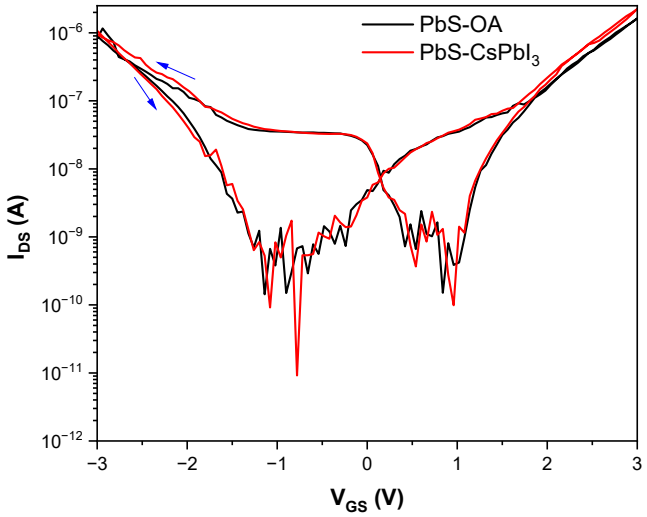

Figure 3.14: Transfer curve in logarithmic scale, for PbS nanocrystals with OA ligands (red) and $CsPbI_3$ ones (black). V_{DS} = 1 V. Forward and reverse sweeps represented with blue arrows.

Having established that perovskite ligands enhance the conduction of carriers, we now aim to determine the optimal number of depositions, as well as the best concentration of the semiconductor material, for a maximum value of mobility - one of the key performance indicators of a TFT.

The above mentioned presence of leakage current will disturb the extracted measurements, nevertheless the overall shape of a field-effect transistor is present. In Figure 3.15 both sweep directions open and close in the same region: at 0.125 V for holes, and 0.313 V for electrons, with low hysteresis noticed, and apparent ambipolar behaviour. Similarly, in Figures 3.16 and 3.17 a clear dual charge carrier transport is present, in which, due to time constraints, only the hole-type one was studied.

Three depositions were found to yield the highest mobility among the tested number of semiconductor layers, which is in agreement with results in [43], where after an initial number of layers, the mobility value will start to saturate. Adding more semiconductor material reduces chances of void spaces in the film, as well as improved chances of hopping between QDs. However, as another layer is added, phenomena such as incomplete solvent evaporation and asymmetric deposition of the extra layer will induce more trapping spaces, decreasing the overall mobility of the layer. The new addition of solvent to the already established layer will also re-disperse the semiconductor material, further affecting the established molecular packing and accentuating the asymmetry of the layer [44][45]. Assessing the uncertainty of the mobility value for 1 deposition of 26 mg $\cdot$ mL^{-1}, we found it to be 5.1×10^{-5} cm^2 $\cdot$ V^{-1}s^{-1}, one order of magnitude below the measured mobility value.

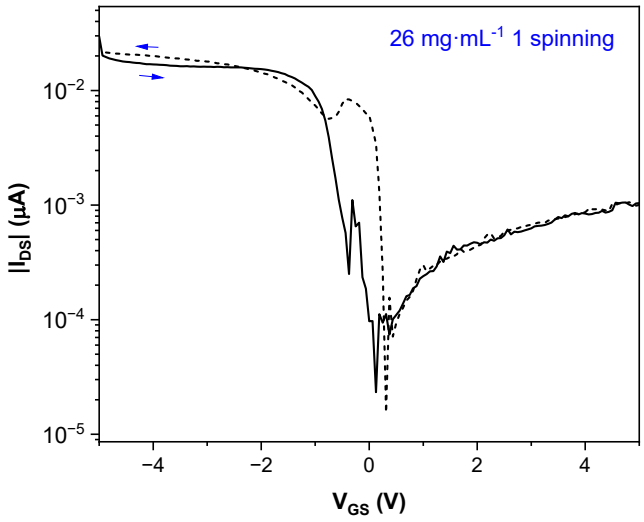

Figure 3.15: Transfer curves for 1 deposition of 26 mg $\cdot$ mL^{-1} LE QDs. V_{DS} = 1 V. Forward and reverse sweeps represented with blue arrows.

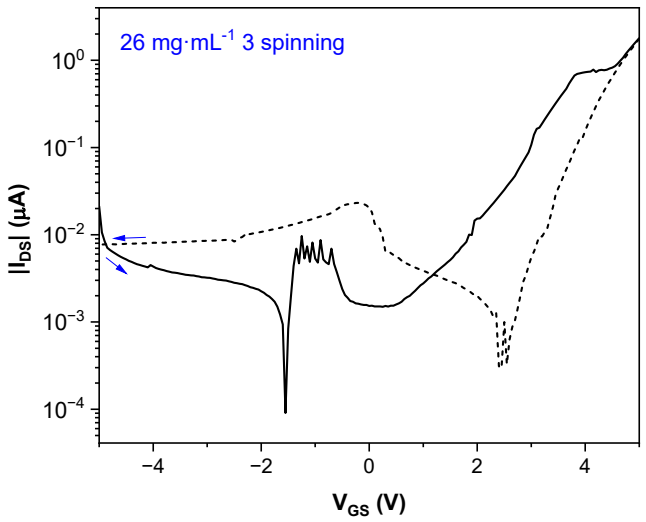

Figure 3.16: Transfer curves for 3 depositions of 26 mg·mL^{-1} LE QDs. $V_{DS} = 0.1$ V. Forward and reverse sweeps represented with blue arrows.

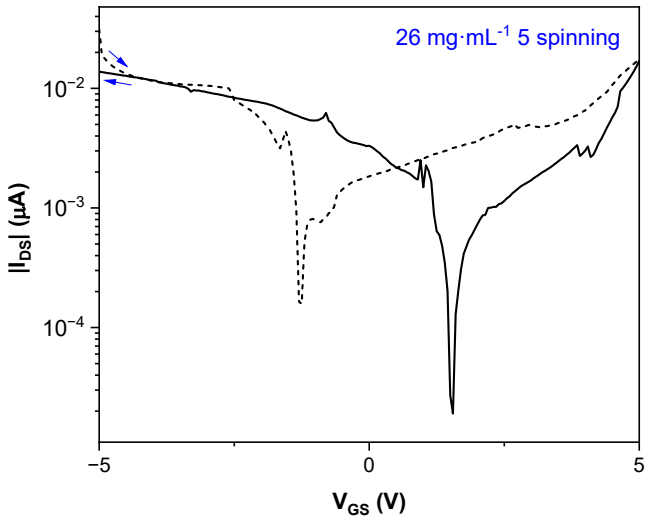

Figure 3.17: Transfer curves for 5 depositions of 26 mg·mL^{-1} LE QDs. $V_{DS} = 0.1$ V. Forward and reverse sweeps represented with blue arrows.

After varying the number of depositions, it is now necessary to study the best concentration of the semiconductor material: In Figure 3.18, I_{DS}-V_{GS} with one deposition of 54 mg $\cdot$ mL^{-1} and 104 mg $\cdot$ mL^{-1} on the left and right, respectively. The 26 mg $\cdot$ mL^{-1} is not displayed as it is already present in Table 3.1.

For the 54 mg, a mobility of approximately 2.64 cm^2 $\cdot$ V^{-1}s^{-1} was found, which would place this result among the best devices for hole transport, however, the extremely large difference compared with the 104 mg $\cdot$ mL^{-1} case makes the result seem dubious. Another confirmation of the anomaly of this value is found in Figure 3.18, where the I_{DS} current is several orders of magnitude than its studied counterparts. Among the explanations for this abnormality, are a possible improper placement of the measuring tips in the semiconductor analyser device, piercing through the dielectric layer, or a bad dispersion of the semiconductor material, not having any thickness in the zone of the wafer where the measurement was conducted.

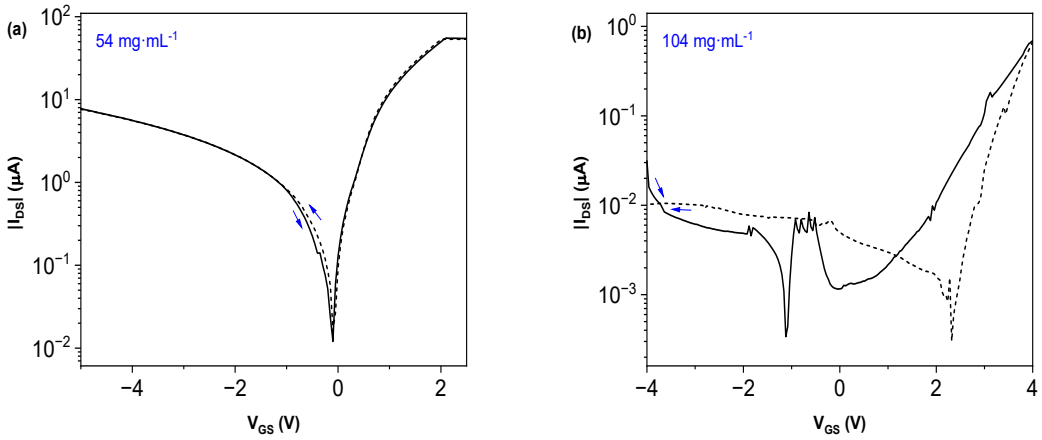

Figure 3.18: Transfer curves for 1 deposition of 54 mg $\cdot$ mL^{-1} (a) and 104 mg $\cdot$ mL^{-1} (b) of LE QDs. V_{DS} = - 0.1 V. Forward and reverse sweeps represented with blue arrows.

Finally, values such as I_{on}/I_{off}, mobility, subthreshold swing and threshold voltage are present in Tables 3.1 and 3.2, sub threshold swing values match expected values found in literature, and confirm the previous conclusion of 3 depositions as the optimal number of layers [40]. I_{on}/I_{off} values exhibit large variance with the different cases studied, with the highest value at 1 spin and 26 mg $\cdot$ mL^{-1}. Such accentuated differences have been reported in other concentration studies, such as [46]. The I_{on} value in Figures 3.15, 3.16 and 3.17 remains approximately constant with respect to the parameter varied, with most of the difference in the ratio coming from the I_{off}, suggesting that the increase in concentration and number of layers is, at the same time, leading to a larger amount of trap states and leakage current. Another possibility, similar to what was reported in [2] is the aggregation of the QDs, consequential decrease in their quantum confinement behaviours, acting likewise a highly defective bulk PbS.

With this in mind, of the concentrations displayed and analysed, the 104 mg · mL^{-1} yielded the best mobility, even though with an lower value of I_{on}/I_{off}. A higher concentration will potentially cause a better packing of quantum dots in the film, and consequently better charge transport.

Table 3.1: Extracted electrical parameters for holes as charge carriers with different numbers of depositions.

Nº of spins (26 mg · mL^{-1})	I_{on}/I_{off}	μ_{FE} (cm^2 · V^{-1}s^{-1})	**S** (V · dec^{-1})	V_T (V)
1 Spin	1.355×10^3	3.60×10^{-4}	-0.255	0.125
3 Spins	3.544×10^1	8.81×10^{-2}	-0.113	-1.550
5 Spins	1.223×10^2	8.25×10^{-2}	-0.214	-1.250

Table 3.2: Extracted electrical parameters for different concentrations.

Concentration (mg · mL^{-1})	I_{on}/I_{off}	μ_{FE} (cm^2 ·V^{-1}s^{-1})	**S** (V · dec^{-1})	V_T (V)
54	6.507×10^2	2.64	-0.174	-0.100
104	7.878×10^1	8.33×10^{-2}	-0.269	-1.120

A visual representation of this variation of parameters, both number of spinning and concentration ones, can be found in Figure 3.19, in logarithmic scale.

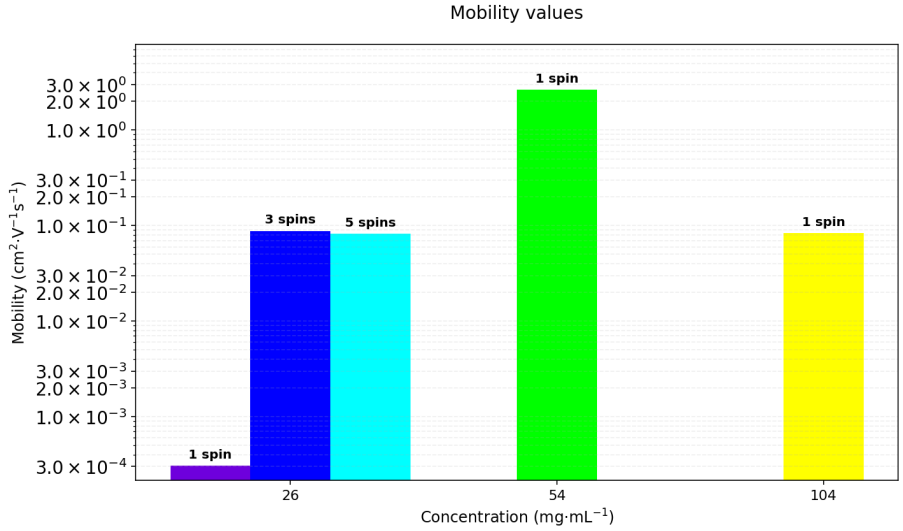

Figure 3.19: Aggregated graph bar with concentration of semiconductor material and number of spinning.

3.4.2.2 I_{DS}-V_{DS} Curves

Figures 3.20 and 3.21 compare the effects of a 10 mW · cm^{-2} light on the I_{DS} current, which, in the same region from -7 to 0 V, increases it by a order of magnitude, demonstrating the effects of photoconductivity. The effects of light in current of the transistor are displayed in Figure I.1 from the annex I.

Another interesting trait of the semiconductor, found on these graphs, is the sharp exponential growth of the current as the voltage goes towards negative values, a clear contrast with Figure 3.22, where we see the traditional n-type output curve. However, this exponential growth is also reported in [3][47].

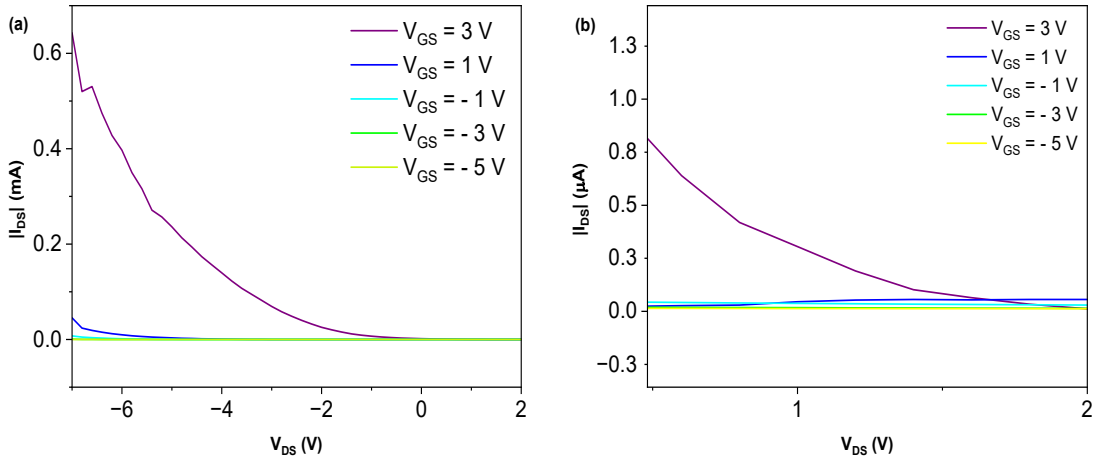

Figure 3.20: Output curves for 3 depositions of 26 mg · mL^{-1} of LE QDs in dark conditions (a) and zoomed section of the graph (b). Different V_{GS} applied.

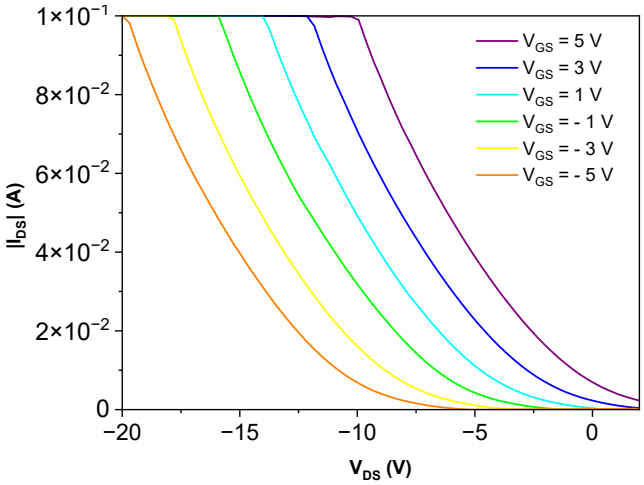

Figure 3.21: Output curve for 3 depositions of 26 mg·mL^{-1} of LE QDs under a 10 mW·cm^{-2} light. Different V_{GS} applied.

In Figure 3.22, taken from a negative to a positive voltage, the expected initial linear growth is seen, followed by the saturation of the transistor.

When comparing the current values between Figures 3.21 and 3.22 we observe that the order of magnitude of the current with holes (negative direction) greatly surpasses the one of the electron (positive direction), a sign that the conduction is being made mostly through holes. Output curves of 54 mg · mL^{-1} and 104 mg · mL^{-1} cases are displayed in the annex I.

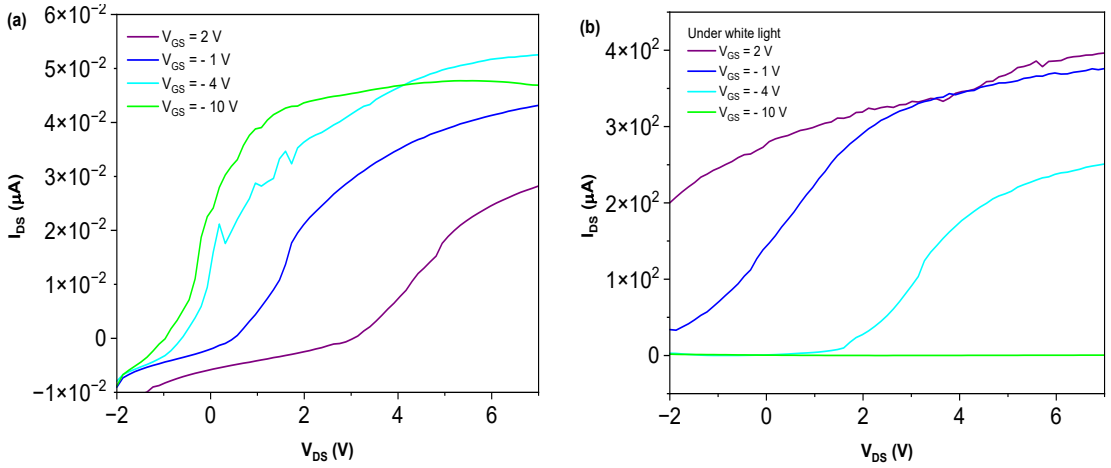

Figure 3.22: Output curves for 5 depositions of 26 mg · mL^{-1} of LE QDs in dark (a) and under a 10 mW · cm^{-2} light (b). Different V_{GS} applied.

To conclude, in Table 3.3, we show the effects of a 10 mW · cm^{-2} light on the previously studied parameters. The mobility of the carriers increased by a factor of 10 for the optimal concentration, and remained approximately constant in terms of the optimal spinning conditions. The biggest change was in terms of I_{on}/I_{off} factor, which increased by a factor of 1000 for both cases.

Table 3.3: Extracted electrical parameters under light, for optimal spinning and concentration.

Optimal (Illuminated)	I_{on}/I_{off}	μ_{FE} (cm^2 · V^{-1}s^{-1})	S (V · dec $^{-1}$)	V_T (V)
3 Spins of 26 mg · mL^{-1}	1.497×10^5	3.459×10^{-2}	-0.476	-1.100
104 mg · mL^{-1}	6.310×10^3	3.690×10^{-1}	-0.298	-0.850

3.4.2.3 Photo-switching Characteristics

By analysing the response of a device to different incident wavelengths, it is possible to take information relative to its stability during consecutive on/off cycles. The graphs in Figure 3.23 were taken inside a Faraday cage in Agilent 4155C, under 10 mW · cm^{-2} light illumination, with 0.5 s intervals, at a fixed $V_{GS} = -3\,V$ and $V_{DS} = 1\,V$. The transient response of both OA and LE QDs TFT under periodic on/off cycles of white light illumination was then investigated.

The change in ligands, from oleic acid to $CsPbI_3$, had a notorious increase in the drain current value, from 1×10^{-8} A to 3×10^{-6} A, a factor of 300.

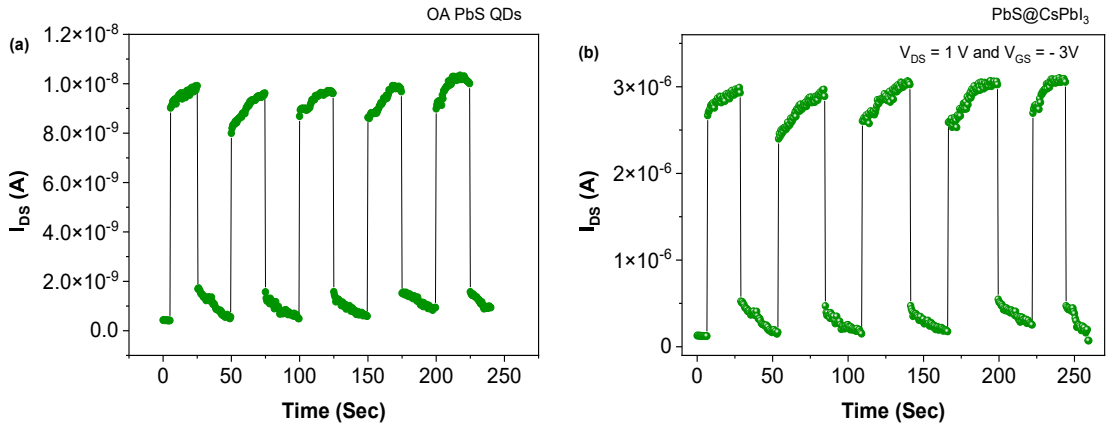

Figure 3.23: On/Off curves of oleic acid terminated PbS QDs (a) and $CsPbI_3$ terminated QDs (b) under 10 mW · cm^{-2}.

An explanation can be the higher charge mobility that perovskite possesses when compared to the carbon chains of oleic acid. Over the experiment, the rise time curves have a consistent behaviour and appearance, indicating the required repeatability and reversibility for the device's functioning, proving that PbS with $CsPbI_3$ terminations can be used as a phototransistor.

The ratio considered for the rise and fall times was 10-90 %.

In terms of the rise and fall times values exhibited in Table 3.4, ours are among average, although towards the higher end of the spectrum [48].

Table 3.4: Specific characteristics of On-Off cycle for $CsPbI_3$-terminated PbS QDs.

	Rise Time (ms)	Fall Time (ms)
On/Off Cycle	50	31

In Figure 3.24 the gate-source voltage applied is varied over time. We notice the p-type behaviour of the semiconductor layer, as the voltage becomes more negative, the bigger the current amplitude is found. This conclusion matches the one found in sub-subchapter 3.4.2.2.

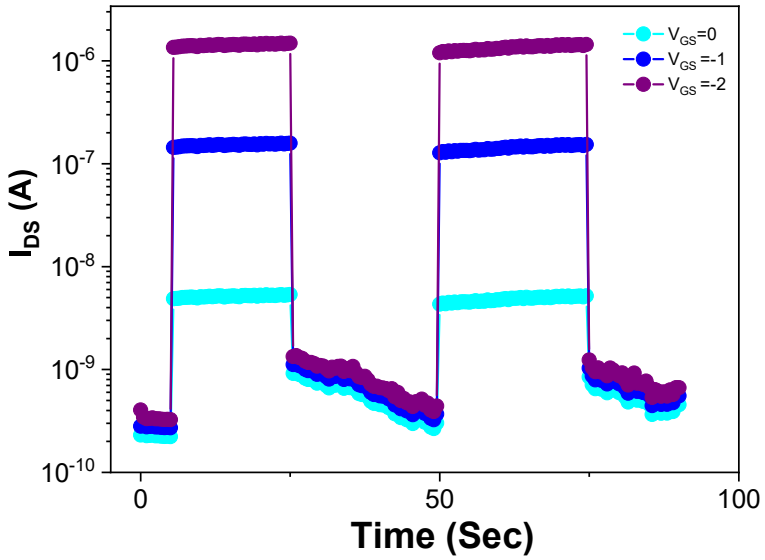

Figure 3.24: I_{DS} current over time for 26 mg · mL^{-1} PbS QDs with $CsPbI_3$ terminations. V_{DS} = 1 V

Another key property is the electrical output (P_{light}) per optical input (I_{photo}); Responsivity of the device, which was calculated using Equation 3.3, to be 152.55 A·W^{-1}, a standard value among recent values from PbS based devices [12].

$$R = \frac{I_{photo}}{P_{light}} \tag{3.3}$$

4

CONCLUSION AND PERSPECTIVES FOR THE FUTURE

In this work, the use of PbS QDs with $CsPbI_3$ terminations as the semiconductor layer of a TFT was explored, with the aim of improving the stability, efficiency, and overall capabilities of the devices. The work was initiated with the fabrication of OA PbS QDs through hot-injection synthesis, followed by a ligand exchange process from OA to $CsPbI_3$.

Afterwards, the NC were spin-coated onto a Si substrate covered by an Al_2O_3 dielectric layer. Following this, the final device was fabricated, and several optical, morphological, and electrical characterizations were performed to gain insights into both the devices and the QDs.

4.1 Significance of the Results

The use of the perovskite ligands has shown an increase in the conductivity of the device when compared with its pristine version. The I-V curves and on/off cycles exhibited higher current values with the LE version, indicating an improvement in conductivity, mainly with holes as charge carriers. SEM images present a uniform, coherent layer of QDs, signifying repeatability of the device and uniformity in performance.

Through XRD analysis, it was confirmed that the LE QDs belong to the *Pm3m*, No. 221 perovskite structure.

Regarding electrical performance, we achieved an I_{on}/I_{off} ratio of 1.355×10^3 for 1 spinning of 26 mg $\cdot$ mL^{-1} in dark conditions and 1.497×10^5 for 5 spins at 26 mg $\cdot$ mL^{-1} in illuminated ones. These values subsequently declined with an increasing number of depositions and higher concentrations, attributed to an additional number in trap states and leakage current. The optimized values of field-effect mobility were found at 104 mg $\cdot$ mL^{-1} with 1 spinning for light conditions and 26 mg $\cdot$ mL^{-1} with 3 depositions for dark ones.

A drawback of the used LE process was the vanishing exciton peak after approximately one month, causing non-radiative recombination, an increase in defect states, poor

interface between LE QDs, and overall damping in power output.

The FTIR analysis indicated the presence of impurity groups in the LE QDs samples, such as OA and CO_2. This characterization did not detect PbS bonds due to the ligand layer surrounding the quantum dots.

The fabricated devices exhibited clear photo-responsive behaviour, with current modulation in response to light exposure. The current increased in the presence of light by a factor of 300, maintaining consistent behaviour across multiple on/off cycles, with a rise time of 34 ms and a fall time of 50 ms.

4.2 Limitations and Challenges

This work encountered several setbacks and limitations throughout its progression.

The fabrication of pristine PbS QDs requires precise control over time, particularly during the injection temperature and the removal of the three-necked flask from the heat source. This step has proven to be crucial, as it significantly impacts the characteristics of the fabricated QDs, including their size and emission properties.

Throughout the entire process, maintaining a contamination-free environment via vacuum conditions was essential. Failure to maintain these conditions led to broadening of the QDs peaks and impurity groups in the solution.

The deposition of LE QDs onto the Al_2O_3 dielectric layer proved challenging and required extensive trial and error to optimize the spinning conditions for successful deposition.

Hall effect characterizations did not yield consistent results. Several issues led to aborted measurements, preventing the acquisition of a complete I-V curve. Consequently, those results were not considered. The primary reasons behind this inconsistency are largely attributed to the difficulty of achieving a uniform distribution of LE QDs on a glass substrate, resulting in a non-uniform thickness, and a poor performance of the existing Hall effect equipment in the laboratory, both of which adversely affected the measurement process.

4.3 Future Pursuits

Beyond this work, the QDs developed were mixed with a $CsPbI_2Br$ perovskite solution to pursue greater stability in a type of perovskite material traditionally considered unreliable. This goal was successfully achieved, as the active phase duration of $CsPbI_2Br$ was prolonged from a few hours to several months. This is, naturally, a subject worth further investigation, and with some extra analysis found in annex A.1. Consequently, a Density Functional Theory (DFT) analysis of this system was initiated to find a theoretical explanation for the underlying mechanisms responsible for this increase in stability, representing a novel approach at the CENIMAT Lab.

The DFT analysis is being conducted using the Quantum Espresso software [49], allowing for a theoretical calculation of the energy levels of both types of QDs (pre and post LE) as well as the perovskite material with and without QDs incorporated.

In practical terms, only the $CsPbI_2Br$ perovskite was successfully simulated, enabling the computation of the Fermi level and the total energy of the system. The complexity of the other molecular systems proved too high for standard computational resources, and the use of a computing cluster has not yet been an option.

Future work will focus on deepening the understanding of DFT analysis and further explore the applications of PbS QDs as the semiconductor layer in TFTs, both independently and embedded within perovskite materials. An interesting feasible application, following the works of G. Ribeiro *et al*. [2], Menda *et al*. [50] and correlated with the simulation work done by M. Alexandre *et al*. [51], would be predicting and optimizing the electronic interactions of PbS QDs as the intermediate band material in a solar cell, particularly in understanding how different ligand exchange procedures and their incorporation influence the density of states, Fermi level alignment, and charge transfer mechanisms.

Some of the activities developed are presented in annex A.2.

Bibliography

[1] J. M. Lourenço. *The NOVAthesis LaTeX Template User's Manual*. NOVA University Lisbon. 2021. URL: https://github.com/joaomlourenco/novathesis/raw/main/template.pdf (cit. on p. i).

[2] G. Ribeiro et al. "Sub-Bandgap Sensitization of Perovskite Semiconductors via Colloidal Quantum Dots Incorporation". In: *Nanomaterials* 13.17 (2023). ISSN: 2079-4991. DOI: 10.3390/nano13172447. URL: https://www.mdpi.com/2079-4991/13/17/2447 (cit. on pp. 1, 9, 28, 37).

[3] R. L. do Espírito Santo Rosa Ferreira. "Metal Halide Perovskite Quantum Dots for Thin-Film Transistors". Master's Dissertation. NOVA School of Science and Technology, NOVA University Lisbon: NOVA University Lisbon, 2021-12. URL: http://hdl.handle.net/10362/141862 (cit. on pp. 1, 30).

[4] D. Schmool. *From the Material Properties of Solids to Nanotechnologies*. Berlin, Boston: Mercury Learning and Information, 2016. ISBN: 9781683923183. DOI: doi:10.1515/9781683923183. URL: https://doi.org/10.1515/9781683923183 (cit. on p. 1).

[5] T. R. Pisanic II, Y. Zhang, and T. H. Wang. "Quantum dots in diagnostics and detection: principles and paradigms". In: *Analyst* 139 (12 2014), pp. 2968–2981. DOI: 10.1039/C4AN00294F. URL: http://dx.doi.org/10.1039/C4AN00294F (cit. on p. 2).

[6] T. Mueller and E. Malic. "Exciton physics and device application of two-dimensional transition metal dichalcogenide semiconductors". In: *npj 2D Materials and Applications* 2.1 (2018-09). ISSN: 2397-7132. DOI: 10.1038/s41699-018-0074-2. URL: http://dx.doi.org/10.1038/s41699-018-0074-2 (cit. on p. 1).

[7] G. Liu et al. "Recent advances of eco-friendly quantum dots light-emitting diodes for display". In: *Progress in Quantum Electronics* 86 (2022), p. 100415. ISSN: 0079-6727. DOI: https://doi.org/10.1016/j.pquantelec.2022.100415. URL: https://www.sciencedirect.com/science/article/pii/S0079672722000404 (cit. on p. 2).

[8] S. Ghimire and V. Biju. "Relations of exciton dynamics in quantum dots to photoluminescence, lasing, and energy harvesting". In: *Journal of Photochemistry and Photobiology C: Photochemistry Reviews* 34 (2018), pp. 137–151. ISSN: 1389-5567. DOI: https://doi.org/10.1016/j.jphotochemrev.2018.01.004. URL: https://www.sciencedirect.com/science/article/pii/S1389556717300746 (cit. on p. 3).

[9] B. Hou et al. "Highly Monodispersed PbS Quantum Dots for Outstanding Cascaded-Junction Solar Cells". In: *ACS Energy Letters* 1.4 (2016). PMID: 28035335, pp. 834–839. DOI: 10.1021/acsenergylett.6b00294. URL: https://doi.org/10.1021/acsenergylett.6b00294 (cit. on p. 2).

[10] J. Tang et al. "Colloidal-quantum-dot photovoltaics using atomic-ligand passivation". In: *Nature materials* 10 (2011-09), pp. 765–71. DOI: 10.1038/nmat3118 (cit. on p. 3).

[11] W. Huang et al. "Size tunable and controllable synthesis of PbS quantum dots for broadband photoelectric response". In: *Optical Materials* 142 (2023), p. 113977. ISSN: 0925-3467. DOI: https://doi.org/10.1016/j.optmat.2023.113977. URL: https://www.sciencedirect.com/science/article/pii/S0925346723005499 (cit. on pp. 3, 13, 19).

[12] R. Saran and R. Curry. "Lead sulphide nanocrystal photodetector technologies". In: *Nature Photonics* 10 (2016-01), pp. 81–92. DOI: 10.1038/nphoton.2015.280 (cit. on pp. 3, 33).

[13] Q. A. Akkerman and L. Manna. "What Defines a Halide Perovskite?" In: *ACS Energy Letters* 5.2 (2020). PMID: 33344766, pp. 604–610. DOI: 10.1021/acsenergylett.0c00039. eprint: https://doi.org/10.1021/acsenergylett.0c00039. URL: https://doi.org/10.1021/acsenergylett.0c00039 (cit. on p. 4).

[14] C. J. Bartel et al. "New tolerance factor to predict the stability of perovskite oxides and halides". In: *Science Advances* 5.2 (2019), eaav0693. DOI: 10.1126/sciadv.aav0693. eprint: https://www.science.org/doi/pdf/10.1126/sciadv.aav0693. URL: https://www.science.org/doi/abs/10.1126/sciadv.aav0693 (cit. on p. 4).

[15] J. S. Manser, J. A. Christians, and P. V. Kamat. "Intriguing Optoelectronic Properties of Metal Halide Perovskites". In: *Chemical Reviews* 116.21 (2016). PMID: 27327168, pp. 12956–13008. DOI: 10.1021/acs.chemrev.6b00136. eprint: https://doi.org/10.1021/acs.chemrev.6b00136. URL: https://doi.org/10.1021/acs.chemrev.6b00136 (cit. on p. 4).

[16] S. Thomson. "Observing Phase Transitions in a Halide Perovskite Using Temperature Dependent Photoluminescence Spectroscopy Applications of Fluorescence Spectroscopy View project A P P L I C A T I O N N O T E Observing Phase Transitions in a Halide Perovskite Using Tem". In: *Edinburgh Instruments* May (2018),

pp. 3–6. URL: https://www.researchgate.net/publication/325314706 (cit. on p. 4).

[17] Y.-T. Huang et al. "Perovskite-inspired materials for photovoltaics and beyond—from design to devices". In: *Nanotechnology* 32.13 (2021-01), p. 132004. DOI: 10.1088/1361-6528/abcf6d. URL: https://dx.doi.org/10.1088/1361-6528/abcf6d (cit. on p. 4).

[18] S. Mariotti et al. "Stability and Performance of CsPbI 2 Br Thin Films and Solar Cell Devices". In: *ACS Applied Materials Interfaces* 10 (2018-01). DOI: 10.1021/acsami.7b14039 (cit. on p. 5).

[19] K. Zheng et al. "Improved phase stability of CsPbIBr perovskite by released microstrain toward highly efficient and stable solar cells". In: *InfoMat* 3.12 (2021), pp. 1431–1444. DOI: https://doi.org/10.1002/inf2.12246. eprint: https://onlinelibrary.wiley.com/doi/pdf/10.1002/inf2.12246. URL: https://onlinelibrary.wiley.com/doi/abs/10.1002/inf2.12246 (cit. on p. 5).

[20] M. Grundmann. *The Physics of Semiconductors: An Introduction Including Devices and Nanophysics*. 1st ed. Published: 22 November 2006. Copyright: Springer-Verlag Berlin Heidelberg 2006. Springer Berlin, Heidelberg, 2006, pp. XXXII, 690. ISBN: 978-3-540-34661-6. DOI: 10.1007/3-540-34661-9 (cit. on p. 5).

[21] M. J. Mirshojaeian Hosseini and R. A. Nawrocki. "A Review of the Progress of Thin-Film Transistors and Their Technologies for Flexible Electronics". In: *Micromachines* 12.6 (2021). ISSN: 2072-666X. DOI: 10.3390/mi12060655. URL: https://www.mdpi.com/2072-666X/12/6/655 (cit. on p. 5).

[22] E. Fortunato, P. Barquinha, and R. Martins. "ChemInform Abstract: Oxide Semiconductor Thin-Film Transistors: A Review of Recent Advances". In: *Advanced materials (Deerfield Beach, Fla.)* 24 (2012-08), pp. 2945–86. DOI: 10.1002/adma.201103228 (cit. on pp. 5, 6, 8).

[23] S. R. Thomas, P. Pattanasattayavong, and T. D. Anthopoulos. "Solution-processable metal oxide semiconductors for thin-film transistor applications". In: *Chem. Soc. Rev.* 42 (16 2013), pp. 6910–6923. DOI: 10.1039/C3CS35402D. URL: http://dx.doi.org/10.1039/C3CS35402D (cit. on p. 5).

[24] B. Razavi. *Fundamentals of Microelectronics*. 2nd. Hoboken, NJ, USA: John Wiley & Sons, 2013. ISBN: 978-1-118-15732-2 (cit. on pp. 6, 7).

[25] P. M. C. Barquinha. "Transparent Oxide Thin-Film Transistors: Production, Characterization and Integration". Accessed: 2025-01-28. Doctoral dissertation. Lisbon, Portugal: Universidade Nova de Lisboa, Faculdade de Ciências e Tecnologia, 2010. URL: http://hdl.handle.net/10362/5380 (cit. on p. 7).

[26] X. Zhang et al. "Inorganic CsPbI3 Perovskite Coating on PbS Quantum Dot for Highly Efficient and Stable Infrared Light Converting Solar Cells". In: *Advanced Energy Materials* 8 (2017-10). DOI: 10.1002/aenm.201702049 (cit. on p. 10).

[27] S. Zheng et al. "PbS Colloidal Quantum Dot Inks for Infrared Solar Cells". In: *iScience* 23.11 (2020), p. 101753. ISSN: 2589-0042. DOI: https://doi.org/10.1016/j.isci.2020.101753. URL: https://www.sciencedirect.com/science/article/pii/S2589004220309500 (cit. on p. 10).

[28] E. Carlos et al. "Boosting Electrical Performance of High- Nanomultilayer Dielectrics and Electronic Devices by Combining Solution Combustion Synthesis and UV Irradiation". In: *ACS Applied Materials Interfaces* 9 (2017-11). DOI: 10.1021/acsami.7b11752 (cit. on pp. 10, 22).

[29] I. Moreels et al. "Size-Dependent Optical Properties of Colloidal PbS Quantum Dots". In: *ACS Nano* 3.10 (2009). PMID: 19780530, pp. 3023–3030. DOI: 10.1021/nn900863a. eprint: https://doi.org/10.1021/nn900863a. URL: https://doi.org/10.1021/nn900863a (cit. on p. 14).

[30] L. Bicelli. "A review on photoluminescence and electroluminescence of semiconductors for photoelectrochemical cells". In: *Surface Technology* 26.2 (1985), pp. 93–105. ISSN: 0376-4583. DOI: https://doi.org/10.1016/0376-4583(85)90001-9. URL: https://www.sciencedirect.com/science/article/pii/0376458385900019 (cit. on p. 17).

[31] O. Voznyy et al. "Origins of Stokes Shift in PbS Nanocrystals". In: *Nano Letters* 17 (2017-10). DOI: 10.1021/acs.nanolett.7b01843 (cit. on p. 17).

[32] A. A. Bunaciu, E. UdriŞTioiu, and H. Aboul-Enein. "X-Ray Diffraction: Instrumentation and Applications". In: *Critical reviews in analytical chemistry / CRC* 45 (2015-04). DOI: 10.1080/10408347.2014.949616 (cit. on p. 19).

[33] Q. Shen et al. "Slow hot carrier cooling in cesium lead iodide perovskites". In: *Applied Physics Letters* 111.15 (2017-10), p. 153903. DOI: 10.1063/1.4991993. URL: https://hal.science/hal-01615037 (cit. on p. 19).

[34] G. Bellisola and C. Sorio. "Infrared spectroscopy and microscopy in cancer research and diagnosis". In: *American journal of cancer research* 2 (2012-01), pp. 1–21 (cit. on p. 19).

[35] J. Poppe et al. "A versatile approach for coating oxidic surfaces with a range of nanoparticulate materials". In: *J. Mater. Chem. C* 1 (2013-01), pp. 1515–1524. DOI: 10.1039/C2TC00863G (cit. on p. 20).

[36] B. C. Smith. "The Infrared Spectra of Polymers II: Polyethylene". In: *Spectroscopy* 36.9 (2021-09), pp. 24–29. DOI: 10.56530/spectroscopy.xp7081p7. URL: https://www.spectroscopyonline.com/view/the-infrared-spectra-of-polymers-ii-polyethylene (cit. on p. 20).

[37] F. Rolle and M. Sega. "Use of FTIR spectroscopy for the measurement of CO 2 carbon stable isotope ratios". In: 2019-01, p. 05002. DOI: 10.1051/metrology/201905002 (cit. on p. 20).

[38] A. Mohammed and A. Abdullah. "Scanning Electron Microscopy (SEM): A Review". In: 2019-01 (cit. on p. 21).

[39] Q. X. Zhang. "The Electrical Performances and Leakage Current Conduction Mechanism of Al2O3/ZrO2/SiO2/ZrO2/Al2O3 MIM Capacitors". In: *Integrated Ferroelectrics* 217.1 (2021), pp. 233–239. DOI: 10.1080/10584587.2021.1911316. eprint: https://doi.org/10.1080/10584587.2021.1911316. URL: https://doi.org/10.1080/10584587.2021.1911316 (cit. on p. 22).

[40] S. Sze and K. Ng. "Physics of Semiconductor Devices: Third Edition". In: *Physics of Semiconductor Devices: Third Edition* (2006-04), pp. 1–815. DOI: 10.1002/9780470068328 (cit. on pp. 22, 28).

[41] P. Wiśniewski and B. Majkusiak. "Charge-Trapping-Induced Hysteresis Effects in Highly Doped Silicon Metal-Oxide-Semiconductor Structures". In: *Materials (Basel)* 15.8 (2022), p. 2733. ISSN: 1996-1944. DOI: 10.3390/ma15082733. URL: https://doi.org/10.3390/ma15082733 (cit. on p. 25).

[42] T. Zhang et al. "Understanding the Relationship between Ion Migration and the Anomalous Hysteresis in High-Efficiency Perovskite Solar Cells: A Fresh Perspective from Halide Substitution". In: *Nano Energy* 26 (2016-06). DOI: 10.1016/j.nanoen.2016.05.052 (cit. on p. 25).

[43] S. Z. Bisri et al. "Low driving voltage and high mobility ambipolar field-effect transistors with PbS colloidal nanocrystals". In: *Advanced materials (Deerfield Beach, Fla.)* 25.31 (2013-08), pp. 4309–4314. ISSN: 0935-9648. DOI: 10.1002/adma.201205041. URL: https://pure.rug.nl/ws/files/2364723/2013AdvMaterBisri.pdf (cit. on p. 26).

[44] Q. Liu et al. "Influence of Airflow Disturbance on the Uniformity of Spin Coating Film Thickness on Large Area Rectangular Substrates". In: *Coatings* 12.9 (2022). ISSN: 2079-6412. DOI: 10.3390/coatings12091253. URL: https://www.mdpi.com/2079-6412/12/9/1253 (cit. on p. 26).

[45] Y. Yuan et al. "Ultra-High Mobility Transparent Organic Thin Film Transistors Grown by an off-Centre Spin-Coating Method". In: *Nature communications* 5 (2014-01), p. 3005. DOI: 10.1038/ncomms4005 (cit. on p. 26).

[46] H. You. "Transistor Characteristics of Zinc Oxide Active Layers at Various Zinc Acetate Dihydrate Solution Concentrations of Zinc Oxide Thin-film". In: *Journal of Applied Research and Technology* 13.2 (2015), pp. 291–296. ISSN: 1665-6423. DOI: https://doi.org/10.1016/j.jart.2015.06.003. URL: https://www.sciencedirect.com/science/article/pii/S1665642315000048 (cit. on p. 28).

[47] D. M. Balazs et al. "Colloidal Quantum Dot Inks for Single-Step-Fabricated Field-Effect Transistors: The Importance of Postdeposition Ligand Removal". In: *ACS Applied Materials & Interfaces* 10.6 (2018). PMID: 29368501, pp. 5626–5632. DOI: 10.1021/acsami.7b16882. eprint: https://doi.org/10.1021/acsami.7b16882. URL: https://doi.org/10.1021/acsami.7b16882 (cit. on p. 30).

[48] X. Yin et al. "PbS QD-based photodetectors: future-oriented near-infrared detection technology". In: *J. Mater. Chem. C* 9 (2 2021), pp. 417–438. DOI: 10.1039/D0TC04612D. URL: http://dx.doi.org/10.1039/D0TC04612D (cit. on p. 32).

[49] P. Giannozzi et al. "Advanced capabilities for materials modelling with Quantum ESPRESSO". In: *Journal of Physics: Condensed Matter* 29.46 (2017-10), p. 465901. DOI: 10.1088/1361-648X/aa8f79. URL: https://dx.doi.org/10.1088/1361-648X/aa8f79 (cit. on p. 37).

[50] U. D. Menda et al. "Thermal-Carrier-Escape Mitigation in a Quantum-Dot-In-Perovskite Intermediate Band Solar Cell via Bandgap Engineering". In: *ACS Photonics* 10.10 (2023-09), pp. 3647–3655. ISSN: 2330-4022. DOI: 10.1021/acsphotonics.3c00738. URL: http://dx.doi.org/10.1021/acsphotonics.3c00738 (cit. on p. 37).

[51] M. Alexandre et al. "Light management with quantum nanostructured dots-in-host semiconductors". In: *Light: Science Applications* 10 (2021-11), pp. 2047–7538. DOI: 10.1038/s41377-021-00671-x (cit. on p. 37).

A

Parallel activities developed during the thesis period

During the course of this thesis, we have also focused our attention toward the vast applications of density functional theory and the relation between the produced QDs and Perovskite hosts, which, even though interesting, were not included in the main body of the thesis, but are shown here.

A.1 $CsPbI_2Br$ Perovskite matrix hosting PbS QDs

We verified that the presence of LE PbS QDs stabilizes a traditionally unstable $CsPbI_2Br$ perovskite matrix.

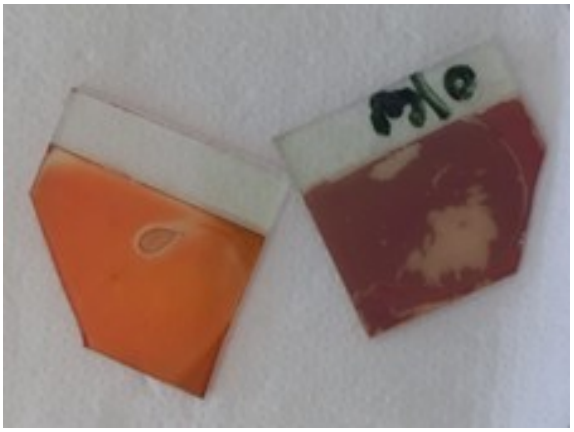

Figure A.1: $CsPbI_2Br$ perovskite with (left) and without (right) LE PbS QDs inserted. 1 h after deposition.

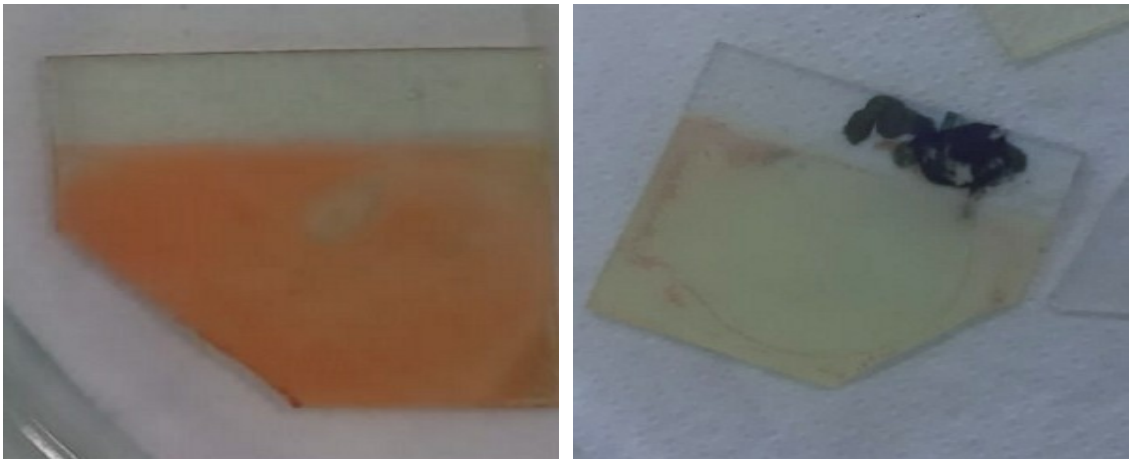

Figure A.2: CsPbI$_2$Br perovskite with (left) and without (right) LE PbS QDs inserted. 48 h after deposition.

A.2 Introductory DFT

In a very introductory approach to density functional theory analysis, we have simulated band diagrams, density of states, among other key properties from different atomic scale systems.

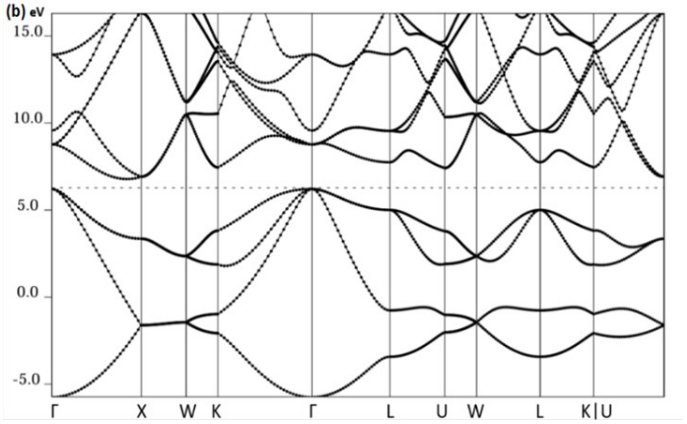

Figure A.3: Band diagrams of silicon with Brillouin zone path as x-axis.

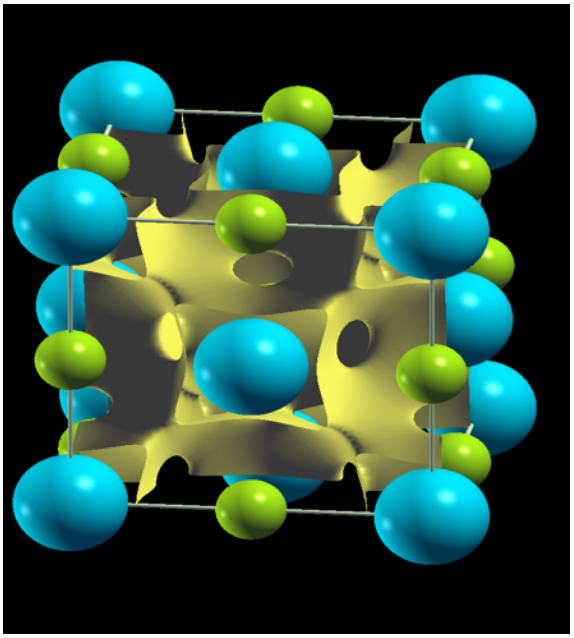

Figure A.4: Isopotential values for an electronic density difference of 0.1 electrons $\cdot$ Å^{-3} in a sodium (green) chloride (blue) molecule.

A.3 Concentration of PbS QDs in Different Solvents

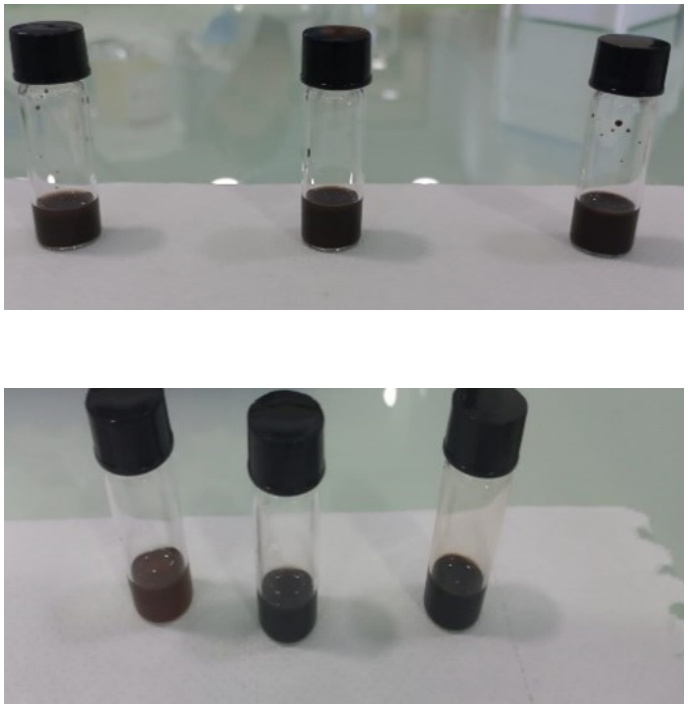

Figure A.5: LE PbS QDs at 10 $mg \cdot mL^{-1}$, 25 $mg \cdot mL^{-1}$, 50 $mg \cdot mL^{-1}$ in propylene carbonate immediately after mixing (up) and after 2 weeks (down).

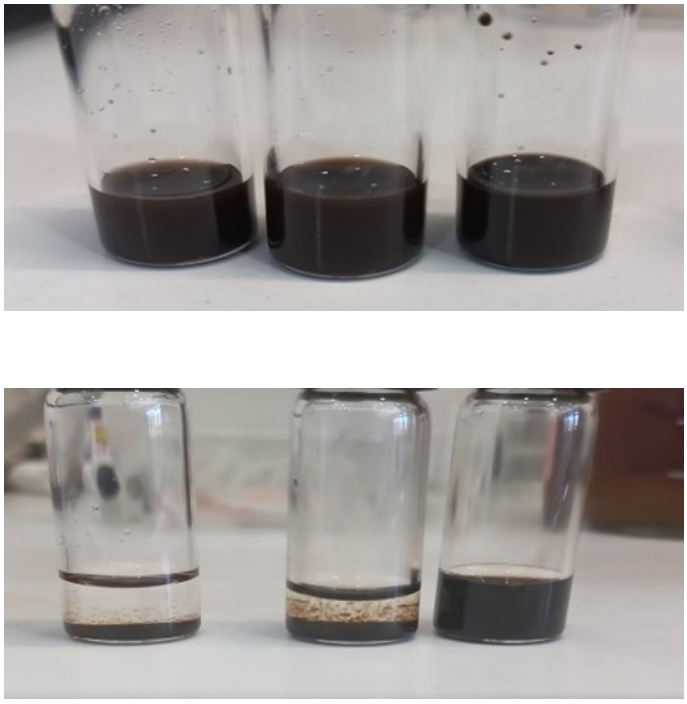

Figure A.6: LE PbS QDs at 10 mg $\cdot$ mL^{-1}, 25 mg $\cdot$ mL^{-1}, 50 mg $\cdot$ mL^{-1} in DMF immediately after mixing (up) and after 2 weeks (down).

B

HOT INJECTION METHOD SET UP, SYNTHESIS AND LIGAND EXCHANGED PRODUCT

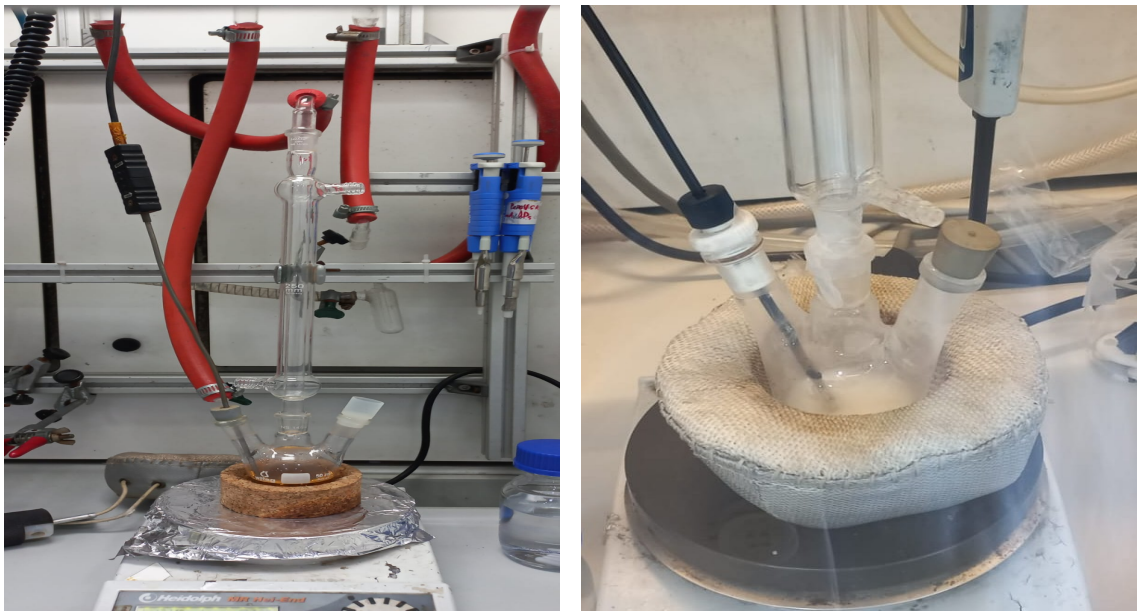

Figure B.1: Hotte environment where the PbS QDs batches were synthesized (left) and (right) three-necked round-bottom flask with lead oleate solution, vacuum tube and temperature sensor.

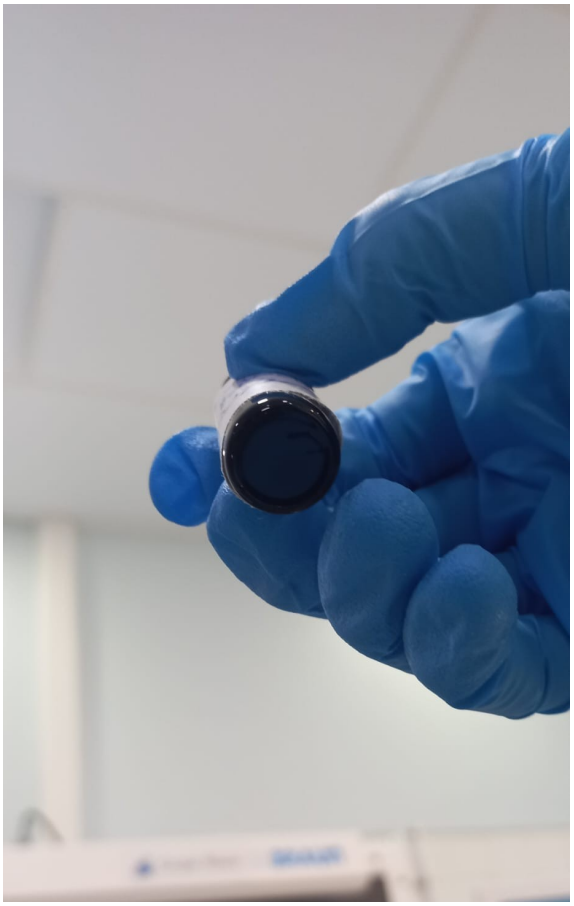

Figure B.2: Oleic acid batch of PbS QDs.

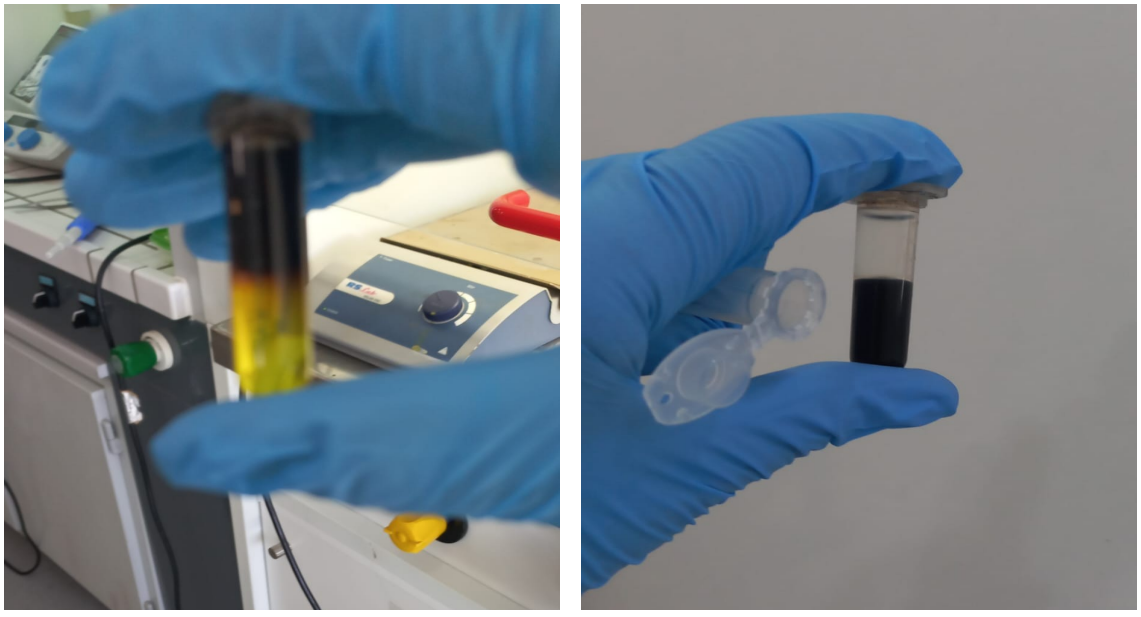

Figure B.3: PbS QDs batches with oleic acid terminations with the ligand exchange precursor solution (left) and LE solution after completion (right).

I

TFT CHARACTERIZATION

I.1 Additional I_{DS}-V_{GS} Transfer Curves

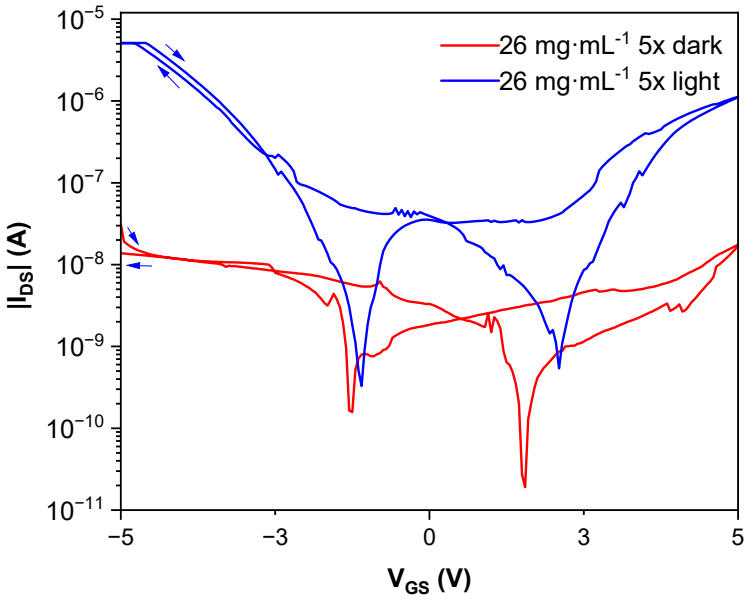

Figure I.1: I_{DS}-V_{GS} curve with photo-enhancement of current present. Both curves at V_{DS} = 0.15 V. Forward and reverse sweeps represented with blue arrows.

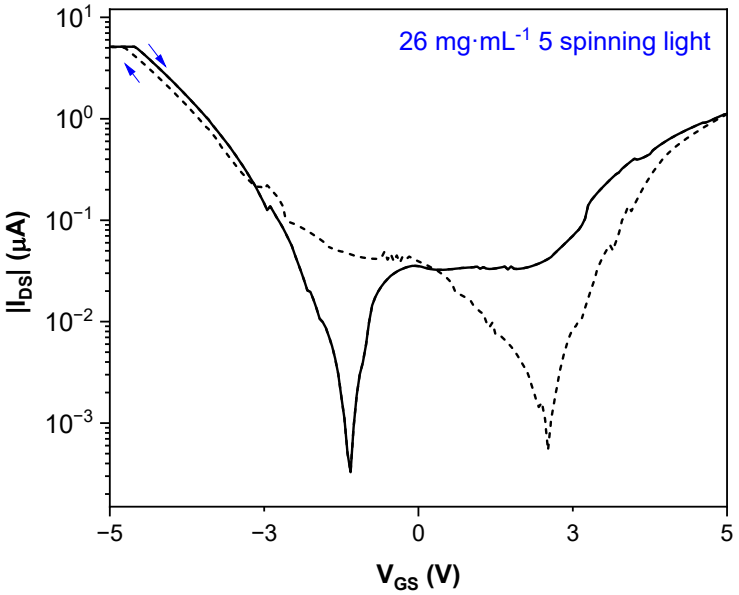

Figure I.2: I_{DS}-V_{GS} curve under light. $V_{DS} = 0.1$ V. Forward and reverse sweeps represented with blue arrows.

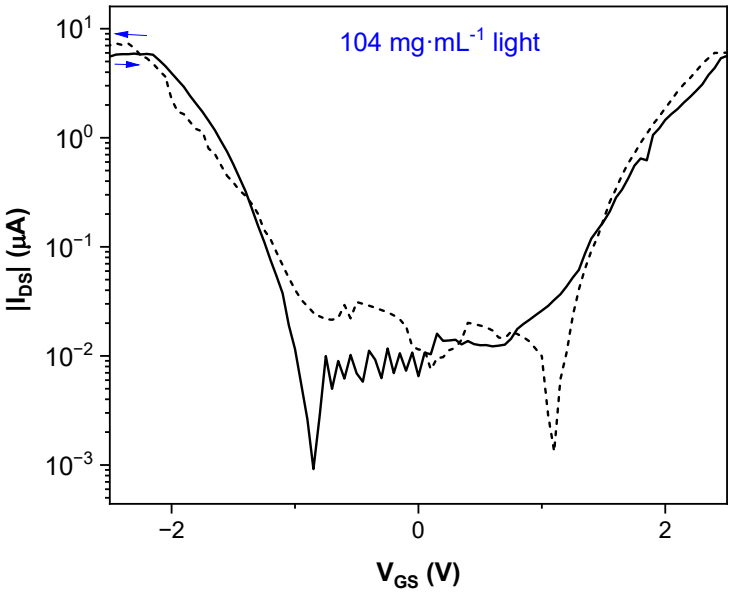

Figure I.3: I_{DS}-V_{GS} curve under light. $V_{DS} = 0.1$ V. Forward and reverse sweeps represented with blue arrows.

I.2 Additional I_{DS}-V_{DS} Output Curves

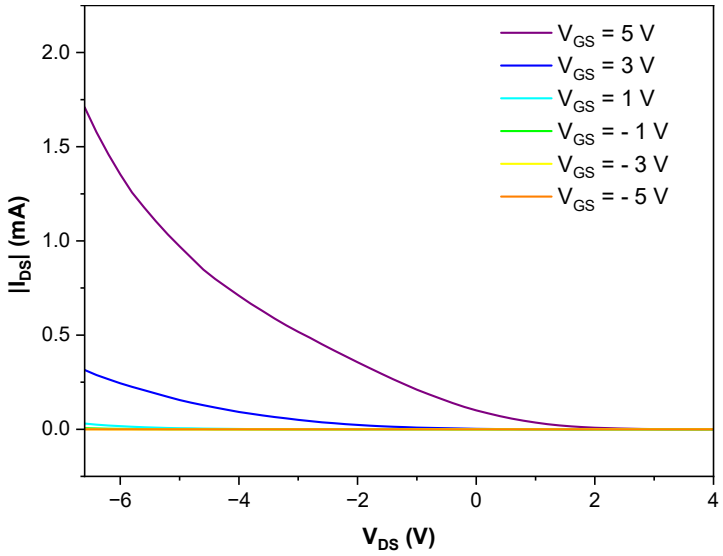

Figure I.4: I_{DS}-V_{DS} output curve of 104 mg · mL^{-1} LE QDs with 1 spin coating deposition. Under dark conditions. Different V_{GS} applied.

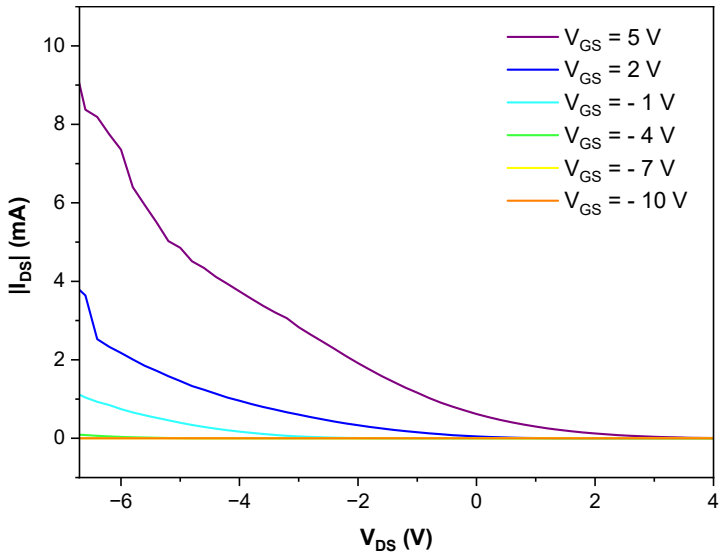

Figure I.5: I_{DS}-V_{DS} output curve of 54 mg · mL^{-1} LE QDs with 1 spin coating deposition. Under dark conditions. Different V_{GS} applied.

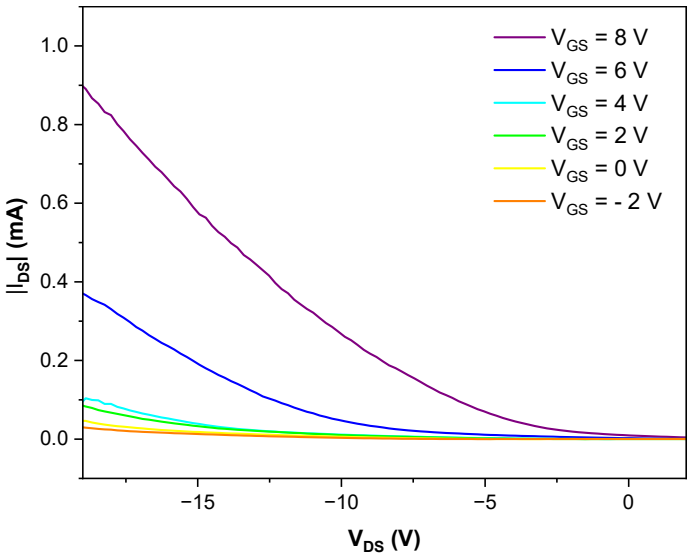

Figure I.6: I_{DS}-V_{DS} output curve of 26 mg · mL^{-1} LE QDs with 5 spin coating depositions. Under dark conditions. Different V_{GS} applied.

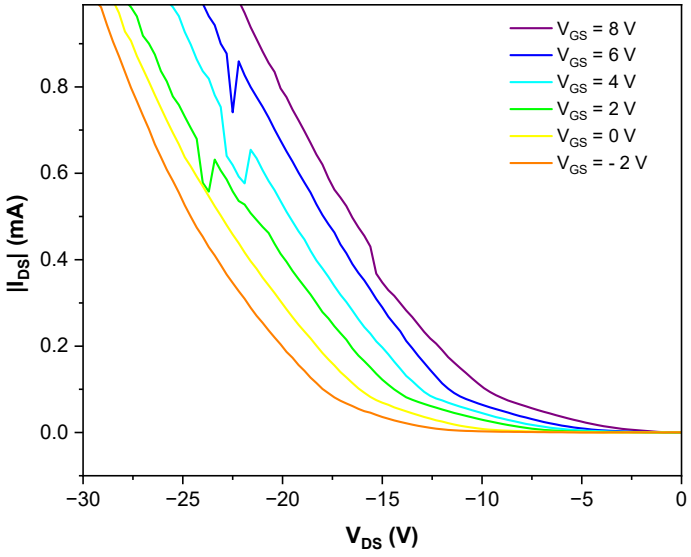

Figure I.7: I_{DS}-V_{DS} output curve of 26 mg · mL^{-1} LE QDs with 1 spin coating deposition. Under dark conditions. Different V_{GS} applied.